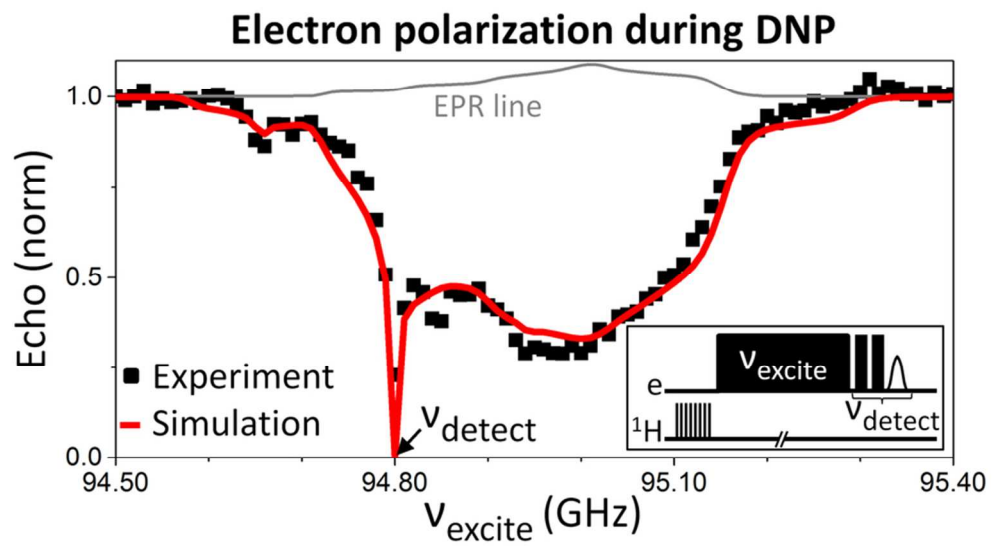




The Electron Depolarization during Dynamic Nuclear Polarization: Measurements and Simulations

Journal:	<i>Physical Chemistry Chemical Physics</i>
Manuscript ID:	CP-ART-08-2014-003825.R1
Article Type:	Paper
Date Submitted by the Author:	12-Oct-2014
Complete List of Authors:	Hovav, Yonatan; Weizmann Institute of Science, Chemical Physics Kaminker, Ilia; Weizmann Institute of Science, Chemical Physics Shimon, Daphna; Weizmann Institute of Science, Chemical Physics Feintuch, Akiva; Weizmann Institute of Science, Chemical Physics Goldfarb, Daniella; Weizmann Institute of Science, Chemical Physics Department Vega, Shimon; Weizmann Institute of Science, Department of Chemical Physics



40x22mm (600 x 600 DPI)

Measurements and simulations of the electron spin polarization along the EPR spectrum of TEMPOL and trityl radicals, under DNP conditions

The Electron Depolarization during Dynamic Nuclear Polarization: Measurements and Simulations

Hovav Y., Kaminker I., Shimon D., Feintuch A., Goldfarb D., and Vega S.*

Weizmann institute of Science, Rehovot , Israel

*shimon.vega@weizmann.ac.il

Abstract

Dynamic nuclear polarization is typically explained either using microscopic systems, such as in the Solid Effect and Cross Effect mechanisms, or using the macroscopic formalism of spin temperature which assumes that the state of the electrons can be described using temperature coefficients, giving rise to the Thermal Mixing mechanism. The distinction between these mechanisms is typically done by measuring the DNP spectrum - i.e. the nuclear enhancement profile as a function of irradiation frequency. In particular, we have previously used the Solid Effect and Cross Effect mechanisms to explain temperature dependent DNP spectra. Our past analysis has however neglected the effect of depolarization of the electrons resulting from the microwave (MW) irradiation. In this work we concentrate on this electron depolarization process and performed MW electron-electron double resonance (ELDOR) experiments on TEMPOL and trityl frozen solutions, in a 3.34 Tesla magnet and at 2.7-30 K, in order to measure the state of the electron polarization during DNP. The experiments indicate that a significant part of the EPR line is affected by the irradiation due to spectral diffusion. Using a theoretical framework based on rate equations for the polarizations of the different electron spin packets and for those of the nuclei we simulated the various ELDOR line-shapes and reproduced the MW frequency and irradiation time dependence. The obtained electron polarization distribution cannot be described using temperature coefficients as required by the classical Thermal Mixing mechanism, and can therefore not be described by this mechanism. Instead, the theoretical framework presented here for the analysis of the ELDOR data forms a basis for the future interpretation of DNP spectra in combination with EPR measurements.

Dynamic Nuclear Polarization (DNP), Electron Electron Double Resonance (ELDOR), Spin Temperature, Thermal Mixing, Solid Effect.

1 Introduction

The inherently low signal to noise ratio detected in NMR can be dramatically increased by the use of Dynamic Nuclear Polarization (DNP). In this technique the large polarization of unpaired electrons, mainly of stable radicals, is transferred to their neighboring nuclei, typically using continuous wave (cw) microwave (MW) irradiation. This technique has been known for more than 60 years [1, 2, 3], but it has only recently become of high interest to the NMR and MRI community due to the introduction of new technological and methodological developments. These enabled DNP in the solid state to be combined with magic angle spinning (MAS) NMR [4, 5, 6, 7, 8, 9, 10], or with the dissolution DNP methodology [11], which can be combined with high resolution liquid state NMR and MRI.

The fundamental mechanism of DNP is of interest both from the point of view of the basic spin physics, which differs from most pulsed magnetic resonance experiments due to its non-coherent nature, and from a practical point of view - allowing better understanding of the processes that can lead to higher NMR and MRI signals. Three main mechanisms were used over the years to explain DNP in non-conducting solid samples: The Solid Effect (SE) [3], the Cross Effect (CE) [12, 13, 14, 15, 16] and the Thermal Mixing (TM) [17, 18, 19] mechanisms. The SE and CE mechanisms were originally explained based on rate equations for the electron and nuclear polarizations, derived from the microscopic quantum mechanical (QM) description of small spin systems, and taking into account the effects of irradiation using a perturbation approach [20] and the effects of relaxation. This QM description was recently extensively studied for DNP on static [21, 22, 23, 24, 25, 26, 27] and rotating [28, 29, 30] samples. Alternatively, the electron and nuclear polarizations can be considered using the macroscopic concept of spin temperature [31, 32, 20, 33], as used in the TM and SE [17, 34, 35] mechanism in EPR lines broader or narrower than the nuclear Larmor frequency, respectively. In this case the state of the spin system is described using several temperature baths, each associated with a part of the system's Hamiltonian and characterized by its own spin temperature. In particular, the electron polarization in inhomogeneously broadened EPR lines is described using an electron Zeeman temperature and an electron non-Zeeman temperature, with the latter corresponding to the change in the electron polarization across the EPR line.

The DNP mechanism is typically studied based on measurements of the nuclear enhancement as a function of the MW frequency, termed the DNP spectrum. For radicals with an EPR line-width larger than the nuclear Larmor frequency these are interpreted either using the TM mechanism [36, 37, 38, 35, 18, 39, 40, 41, 42, 43, 44] or a combination of the SE and CE mechanisms [45, 46, 47]. There are only a few cases where the existence of spin

temperature was directly detected experimentally [48, 49, 50]. In addition, the DNP results were only rarely analyzed together with EPR data [49, 51], where in both cases spin temperature formalisms were used. In particular, while the SE and CE based analysis of the DNP line-shapes results in good fitting of the experimental line shapes, this model did not take into account the non-thermal distribution of the electron polarization within the EPR line-shape during DNP. This can influence the resulting DNP enhancement when different from its thermal value[21]. As such, much insight on the DNP mechanism can be gained by first measuring the electron polarization distribution during MW irradiation (sometimes called the electron saturation profile) [51, 52, 53, 54, 55]. The latter can be explored using electron-electron double resonance[56] (ELDOR) experiments, where the change in the EPR signal intensity due to a MW irradiation at different frequencies is observed. Such an experiment was performed by Granwehr and Köckenberger [52] on DNP samples containing TEMPOL and trityl radicals, using longitudinally detected EPR at 1.5 K and 3.34 Tesla.

The electron polarization distribution is expected to change from its thermal value due to the MW irradiation on the electronic transitions, and because of the spread of polarization across the EPR line due to the electron spectral diffusion (eSD) process. The latter is used in the context of the TM mechanism to explain the formation of the electron non-Zeeman temperature, when its rate is faster than the electron spin lattice relaxation rate[57, 50, 18, 19]. In addition, it is of much interest in EPR[58, 59, 60, 61, 62], mainly in the context of time dependent echo detection, where it is explained based on electron spin flips which induce stochastic fluctuating dipolar fields at the positions of their neighboring electrons. These electron spin flips are induced by dipolar flip-flop quantum fluctuations, the electron spin lattice relaxation mechanisms, or by hyperfine fluctuations induced by spin diffusion[20, 62].

In this paper the electron polarization distribution of TEMPOL and trityl containing samples under DNP conditions is monitored at 2.7-30 K, using detailed ELDOR measurements performed on a 3.34 Tesla combined pulsed-EPR and NMR spectrometer[63]. The ELDOR line-shapes are analyzed using a theoretical model based on rate equations on the polarizations of the electrons (and nuclei) in the system, resulting in a good agreement between the simulations and the experimental line-shapes. This model includes a QM based description of the electron polarization loss due to (i) MW irradiation on the single quantum (SQ) electronic transitions, and due to (ii) SE DNP type of polarization transfer to the nuclei induced by irradiation on the electron-nucleus zero quantum (ZQ_{en}) and double quantum (DQ_{en}) transitions. In addition it includes the effects of (iii) spin-lattice relaxation as well as a phenomenological description of the (iv) spread of the electron polarization due to the eSD process. The influence of the electron polarization redistribution on the DNP mechanism and specifically on the DNP spectral profiles will be described in upcoming pub-

lications. Finally, we show that the measured electron polarization distribution cannot be described using the spin temperature coefficients, which forms the basis of the classical TM mechanism[64, 50, 35, 18, 44].

2 Experimental

2.1 Sample preparation

Samples were prepared with 15 mM trityl (OX63) radical and 40 mM TEMPOL radical, dissolved in 56/44 wt % mixtures of dimethyl sulfoxide (DMSO) / H₂O. 25 μ l of each solution were placed in a Teflon sample holder for measurement. TEMPOL and DMSO were purchased from Sigma-Aldrich, and the trityl radical from Oxford Instruments.

2.2 The NMR / EPR spectrometer

The experiments were conducted in a 3.34 T field using a combined EPR (95 GHz) and NMR (144 MHz) spectrometer [63], under experimental conditions which were previously used to study DNP enhancements and line-shapes of similar samples [45, 46, 47, 65]. This setup is very flexible in terms of the range of possible sample temperatures and of the MW irradiation duration, and in terms of the range of available excitation and detection frequencies. MW excitation and detection was performed using a home-built bridge with two channels, controlled by the Specman4EPR software package [66]. The radio frequency (RF) excitation and detection are controlled by an APOLLO spectrometer from Tecmag inc., externally triggered by a logic pulse generated by Specman4EPR. The probe-head and sample were located inside a Janis Research inc. liquid helium flow cryostat, and experiments were performed in the temperature range of 2.7-30 K. Reaching 2.7 K required a reduced pressure in the cryostat, which was obtained by pumping.

ELDOR experiment

The ELDOR pulse sequence used is shown schematically in Fig. 1. The experiments were conducted by applying a cw-MW excitation pulse at a frequency ω_{excite} for a duration of t_{excite} using one of the two EPR channels. This was followed by an EPR echo detection using a $\frac{\pi}{2} - \tau_{detect} - \pi$ pulse sequence, with $\frac{\pi}{2}$ pulses of 450 ns, produced by the second channel at ω_{detect} . Prior to each experiment a train of RF pulses was applied on the protons in order to remove their polarization between successive scans. As a result the delay between single experiments could be set to about $5T_{1e}$, where T_{1e} is defined below. The MW amplitude, $\omega_1/2\pi$, was

600 kHz, as measured by a nutation experiment. Due to the low Q of our resonator we assume that this value is uniform over the frequency range used in the experiments. For the experiments performed around 2.7 K the power was reduced, $\omega_1/2\pi = 30$ kHz, in order to limit sample heating within a range smaller than 0.5 K.

The detected signals for a given ω_{excite} and t_{excite} values can be expressed in terms of the electron polarization of the detected electrons prior to the application of the detection pulses, $P_e(\omega_{excite}, t_{excite}, \omega_{detect})$, using:

$$S(\omega_{excite}, t_{excite}, \omega_{detect}) = s(\omega_{detect})P_e(\omega_{excite}, t_{excite}, \omega_{detect}) + b(\omega_{detect}), \quad (1)$$

where $b(\omega_{detect})$ is a baseline artifact contribution to the echo (which can also depend on t_{excite}), which probably originates from pulse ringing. $s(\omega_{detect})$ represents the ω_{detect} dependent proportionality factor between the actual signal and the electron polarization, which depends on the electron concentration and volume, the fraction of electrons contributing to the detected signal (which is EPR line-shape dependent), and the Q factor of the probe. It is possible to normalize the detected signal with respect to the thermal equilibrium signals[52], S_0 , which are detected using the same experimental parameters but with excitation frequencies ω'_{excite} that are situated far outside the EPR spectrum, such that irradiation on them does not have any direct or indirect effect on the detected electrons. In practice $S_0(\omega'_{excite}, t_{excite}, \omega_{detect})$ was evaluated using signal averaging over several ω'_{excite} values. When $b(\omega_{detect})$ is small compared to the signals, S_0 can be used to evaluate the relative saturation of the electrons, $E_e = P_e(t)/P_e(0)$, where $P_e(0)$ is the thermal electron polarization. For electrons positioned around ω_{detect} and MW irradiation at ω_{excite} for a duration of t_{excite} this is given by:

$$E_e(\omega_{excite}, t_{excite}, \omega_{detect}) = S(\omega_{excite}, t_{excite}, \omega_{detect})/S_0(\omega'_{excite}, t_{excite}, \omega_{detect}). \quad (2)$$

When $E_e(\omega_{excite}, t_{excite}, \omega_{detect})$ is one it means that the MW field at ω_{excite} does not affect the detected electrons and when it is zero it indicates full saturation. When $b(\omega_{detect})$ is non negligible Eq. 2 will result in $E_e(\omega_{excite}, t_{excite}, \omega_{detect}) \neq 0$ under full saturation. For clarity, we will define E_{excite} and E_{detect} as the E_e frequency profile obtained using a constant t_{excite} value for either a constant ω_{detect} or a constant ω_{excite} values, respectively. The former shows the dependence of the detected echo on ω_{excite} , as given in a regular echo detected ELDOR experiment, and the latter shows the polarization of the different electrons when irradiating at a certain ω_{excite} frequency. Note that E_{detect} requires measurements at both ω_{excite} and ω'_{excite} , for normalization.

The actual intensity of the EPR spectrum $S^*(\omega_{detect}; \omega_{excite}, t_{excite})$ at the end of a MW ir-

radiation of duration t_{excite} at frequency ω_{excite} can be calculated by multiplying $E_{detect}(\omega_{excite}, t_{excite}, \omega_{detect})$ by the EPR line intensity $f(\omega_{detect})$ for each ω_{detect} :

$$S^*(\omega_{detect}; \omega_{excite}, t_{excite}) = f(\omega_{detect}) * E_{detect}(\omega_{excite}, t_{excite}, \omega_{detect}). \quad (3)$$

This value is proportional to the total electron polarization around the detected frequency.

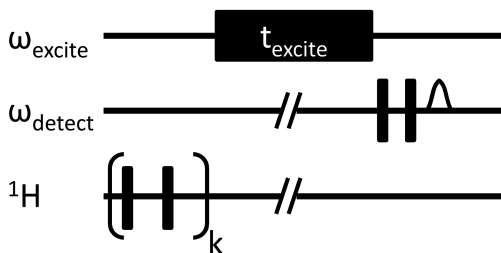


Figure 1: A schematic representation of the ELDOR sequence used. This included a saturation pulse train on the ^1H nuclei, followed by MW irradiation at ω_{excite} for a duration of t_{excite} , and a detection of an echo at a frequency of ω_{detect} . This sequence was then repeated with a delay between scans of about $5T_{1e}$ or longer.

2.3 T_1 measurements

The electron and nuclear relaxation times, T_{1e} and T_{1n} , were determined by analyzing the recovery of the echo intensity after signal saturation by a long cw MW pulse (using $t_{excite} > T_{1e}$) or a RF pulse train, respectively. The NMR recovery curves could be analyzed by a single exponential functions with time constant T_{1n} . The intensity of the EPR echo signals were recorded and fitted using either a single exponential or when required using a double exponential function with the slow (and major) component assigned to T_{1e} . The electron relaxation times were only collected around the frequencies of the maximum EPR line intensity.

3 Experimental results

In this section we show the results of ELDOR measurements on samples containing TEMPOL and trityl radicals as a function of t_{excite} , ω_{detect} , and ω_{excite} . In particular, E_{detect} profiles were measured using t_{excite} irradiation times of the order of T_{1e} in order to allow for a possible electron non Zeeman temperature to form in the system. The spin-lattice relaxation rates of these samples were measured and are summarized in Table 1. For convenience, the values of ω_{excite} and ω_{detect} will be given in frequency units relative to a fixed reference frequency, ω_c , using $\delta\nu_{excite} = (\omega_{excite} - \omega_c)/2\pi$ and $\delta\nu_{detect} = (\omega_{detect} - \omega_c)/2\pi$. The value of $\omega_c/2\pi$ was set

to 95 GHz in the TEMPOL case and to 94.86 GHz in the trityl case, such that ω_c is about equal to the center frequency of the EPR line.

Radical	TEMPOL			Trityl	
Temperature	20 K	7 K	2.7 K	30 K	2.7 K
T_{1e} [ms]	5.5	50	240	32	270
T_{1n} [s]	13	30	220	14	250
t_{excite} [ms]	20	100	1000	100	1000

Table 1: The electron and nuclear relaxation times of the two samples measured at the different temperatures. The lengths of the saturation pulses, t_{excite} , used during the T_{1e} measurements are also given.

3.1 TEMPOL sample

The ELDOR measurements on a 40 mM TEMPOL solid solution were performed at 20 K, 7 K, and 2.7 K. Here the baseline distortions $b(\delta\nu_{detect})$ were significant with respect to the detected echo intensities, causing the detected echo signals to be different from zero even at full saturation conditions, resulting in a distortion of the E_e values calculated using Eq. 2. Fig. 2a shows a contour of $E_e(\delta\nu_{excite}, t_{excite}, \delta\nu_{detect})$ obtained from ELDOR signals for different $\delta\nu_{detect}$ and $\delta\nu_{excite}$ frequencies at 20K, using $t_{excite} = 10$ ms. Individual E_{excite} and E_{detect} profiles are plotted in Fig. 2b and c, respectively. The latter have a lower spectral resolution and are therefore more susceptible to noise and to changes in the experimental $b(\delta\nu_{detect})$ values. The E_{excite} profiles show sharp minima at $\delta\nu_{excite} = \delta\nu_{detect}$, and a broad minima around $\delta\nu_{excite} = 0$. The first minima are a result of on-resonance MW saturation and the second minima is attributed to the eSD mechanism. These broad minima appear in the E_{detect} profiles as an increase of their slopes around $\delta\nu_{excite} = \delta\nu_{detect}$ when $\delta\nu_{excite}$ is moving away from the center of the EPR line. In other words, irradiating at the center affects most of the electron packets composing the EPR line, while irradiation at the side affects only neighboring packets. In addition to these minima, some depolarization is observed for irradiation outside of the EPR line (see for example arrows in Fig. 2b). This is attributed to polarization loss to the ^1H nuclei in the sample due to irradiation on DQ_{en} or ZQ_{en} transitions. The result of MW irradiation on the expected EPR line intensity $S^*(\omega_{detect}; \omega_{excite}, t_{excite})$, defined in Eq. 3, is plotted in Fig. 2d. As can be see, irradiation close to the center of the EPR line results in a large reduction of the total electron polarization, whereas irradiation at the side of the spectrum has a relative small effect on it.

In Fig. 3 E_{excite} spectra obtained for different t_{excite} values using $\delta\nu_{detect} = 0$ are plotted. For short irradiation times the MW irradiation results in a relatively narrow hole which is burned in the E_{excite} spectrum around around $\delta\nu_{excite} = \delta\nu_{detect}$, due to MW irradiation on

the SQ transitions. In addition to this some depolarization can be observed when irradiating around $\delta\nu_{excite} = \delta\nu_{detect} \pm 144$ MHz, corresponding to polarization loss to the nuclei when irradiating on DQ_{en} and ZQ_{en} transitions of the detected electrons. For increasing t_{excite} values the widths of the profile increases and after 50 ms it decreases again to some extent. A steady state profile is reached in a time shorter than 1 s, which is much longer than T_{1e} , indicating that this narrowing effect involves polarization transfer to the 1H and ^{14}N nuclei in the sample [53]. This process is shorter than the nuclear polarization buildup time of the order of 13 s. The ELDOR results obtained at long t_{excite} times were recorded using a single scan, and therefore show a reduced signal to noise ratio (SNR).

In Figs. 4 E_{excite} spectra measured at 7 K (a,b) and 2.7 K (c,d) are plotted as a function for (a,c) several $\delta\nu_{detect}$ frequencies, with $t_{excite} = 0.1$ s at 7 K and 0.5 s at 2.7 K; and (b,d) for several t_{excite} values and $\delta\nu_{detect} = 0$. Once again, at 2.7 K the MW power was reduced and was set to about $\omega_1/2\pi = 30$ kHz. As can be clearly observed, the width of the enhancement profiles broadens with the decrease in temperature, with the effect of the eSD process becoming strong enough to almost saturate the whole EPR line for MW fields applied at any $\delta\nu_{excite}$ frequency inside the EPR line. As before, the saturation profiles reach their maximal width in a timescale comparable to T_{1e} , after which they show a slight narrowing.

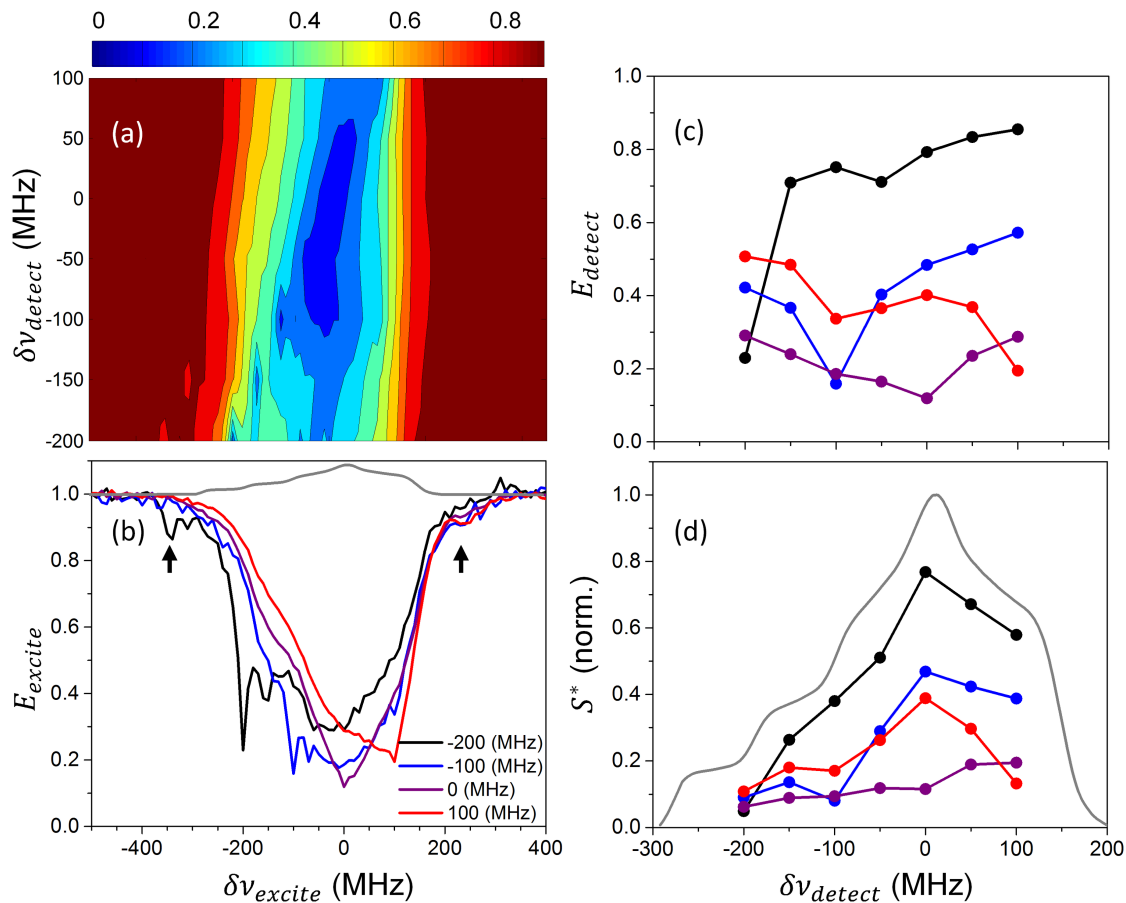


Figure 2: Normalized electron polarizations $E_e(\delta\nu_{excite}, t_{excite}, \delta\nu_{detect})$ measured on the 40 mM TEMPOL sample at 20 K. This was done for a set of excitation and detection frequencies $\nu_{excite} = \nu_0 + \delta\nu_{excite}$ and $\nu_{detect} = \nu_0 + \delta\nu_{detect}$, with $\nu_0 = 95$ GHz, using $t_{excite} = 10$ ms. In (a) the measured data are presented in a contour plot and in (b) and (c) individual $E_{excite}(\delta\nu_{excite})$ and $E_{detect}(\delta\nu_{detect})$ profiles are shown. In (b) the colors of the different profiles correspond to constant $\delta\nu_{detect}$ values that are assigned inside the figure. In (c) the colors of the profiles correspond to constant $\delta\nu_{excite}$ values using the same color codes as defined inside (b). The black arrows in (b) indicate depolarizations due to irradiation outside the EPR spectrum and at the top the EPR spectrum is shown taken from Ref. [45]. In (d) the expected EPR signal intensity $S^*(\delta\nu_{detect}; \delta\nu_{excite}, t_{excite})$ is plotted as a function of $\delta\nu_{detect}$, for different $\delta\nu_{excite}$ values, and has been derived from the EPR line-shape (gray line) and the profiles in (c), as given by Eq. 3.

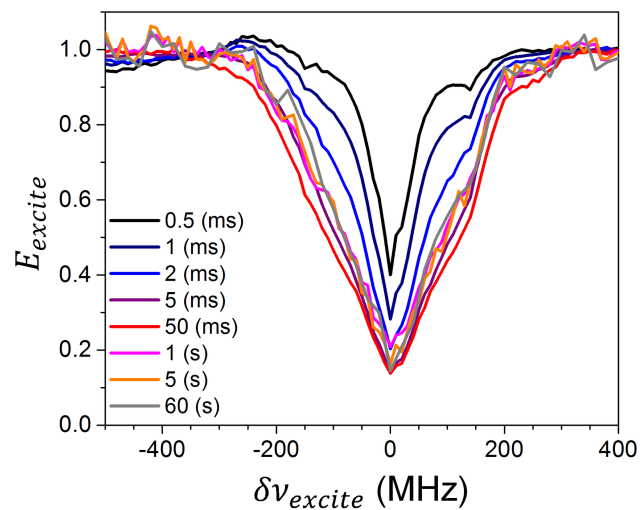


Figure 3: Measured $E_{excite}(\delta\nu_{excite})$ spectra at different t_{excite} values of the 40 mM TEMPOL sample at 20 K for a set of excitation frequencies $\nu_{excite} = \nu_0 + \delta\nu_{excite}$, with $\nu_0 = 95$ GHz, using a detection frequency of $\nu_{detect} = 95$ GHz ($\delta\nu_{detect} = 0$). The t_{excite} values are defined by the color coding inside the figure.

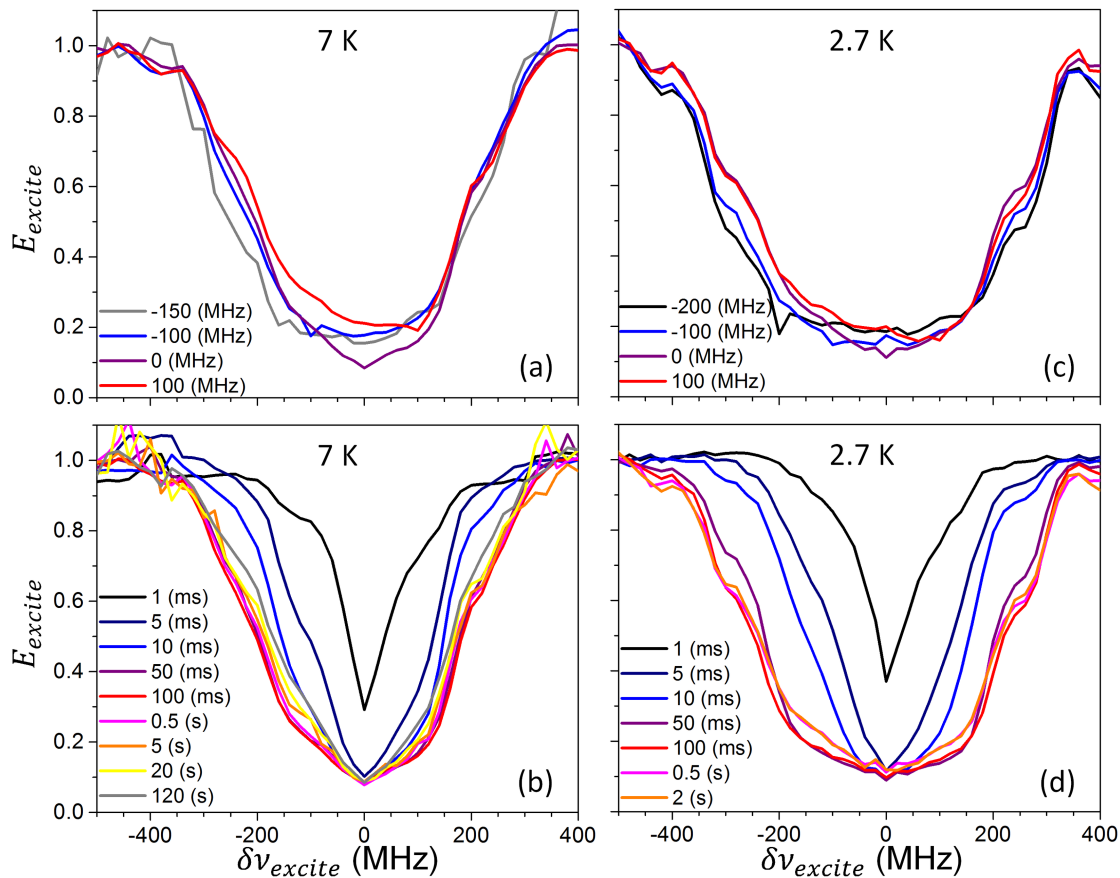


Figure 4: Normalized electron polarizations $E_e(\delta\nu_{excite}, t_{excite}, \delta\nu_{detect})$ measured on the 40 mM TEMPOL sample at 7 K and 2.7 K for a set of excitation and detection frequencies $\nu_{excite} = \nu_0 + \delta\nu_{excite}$ and $\nu_{detect} = \nu_0 + \delta\nu_{detect}$, with $\nu_0 = 95$ GHz. In (a) $E_{excite}(\delta\nu_{excite})$ profiles obtained at 7 K using $t_{excite} = 100$ ms are plotted for different $\delta\nu_{detect}$ values, defined by the color coding inside the figure. In (b) $E_{excite}(\delta\nu_{excite})$ profiles obtained at 7K using $\delta\nu_{detect} = 0$ are plotted for increasing t_{excite} values, defined by the color coding inside the figure. In (c) and (d) similar profiles are plotted as in (a) and (b) but at 2.7K, $\omega_1/2\pi = 30$ kHz instead of 600 kHz, and using $t_{excite} = 500$ ms in (c).

3.2 Trityl sample

The ELDOR measurements on a 15 mM trityl solid solution were performed at 30 K and 2.7 K. The detected echoes were much higher than the baseline artifacts $b(\nu_{detect})$, thus the latter could be neglected. In Fig. 5a the results of the ELDOR experiments at 30 K are summarized by plotting the contour $E_e(\delta\nu_{excite}, t_{excite}, \delta\nu_{detect})$ for $t_{excite} = 0.1$ s. The ELDOR results can be divided into three $\delta\nu_{excite}$ frequency regions: The SQ center region, where the MW irradiation frequencies cover the frequency span of the EPR line, result in a direct saturation of the electrons; and the DQ_{en} and ZQ_{en} frequency regions, which are

removed by $\mp\nu_H$ from the center region, where irradiation on the electron ^{-1}H DQ_{en} and ZQ_{en} transitions results in electron polarization loss due to SE type of polarization transfer to the surrounding nuclei[53]. In addition to this, the polarization loss can spread through the EPR line due to eSD. Polarization loss in the SQ region can also occur due to irradiation on the electron ^{-13}C DQ_{en} and ZQ_{en} transitions, influenced by the hyperfine interaction of the electrons with the natural abundance ^{13}C nuclei of the trityl radicals themselves [67]. This will only be considered in the supplementary information.

We first examine several E_{excite} profiles, as plotted in Fig. 5b. Starting from MW irradiation in the SQ region, clear minima are observed when $\delta\nu_{excite} \cong \delta\nu_{detect}$ and in addition broader minima appear at $\delta\nu_{excite}$ values between $\delta\nu_{detect}$ and zero. Small depolarization and hyperpolarization ($E_{detect} > 1$) effects are also observed when detecting around the edges of the EPR spectrum, as indicated by the black arrows in the figure. The obtained profiles are about antisymmetric with respect to $\delta\nu_{detect} = 0$, reflecting the symmetry of the EPR line-shape. A similar behavior as in the SQ region can be seen when inspecting the smaller depolarization at the DQ_{en} and ZQ_{en} regions. The extra depolarization and hyperpolarization features are not observed here, possibly due to low SNR.

Several E_{detect} profiles are plotted in Fig. 5c., with $\delta\nu_{excite}$ located inside the SQ region. Single minima are found at $\delta\nu_{excite} \cong \delta\nu_{detect}$, and the shapes of these profiles around these minima have faster slopes towards the center EPR frequency than toward the edges of the EPR spectrum. In addition, the inward slopes increase when the $|\delta\nu_{excite}|$ frequencies move away from zero. Once again, electron hyper-polarizations are observed for high $|\delta\nu_{detect}|$ and $|\delta\nu_{excite}|$ values, and the results show an inverse symmetry with respect to $\delta\nu_{excite} = 0$.

The expected EPR signal intensity $S^*(\omega_{detect}; \omega_{excite}, t_{excite})$ as a function of $\delta\nu_{detect}$ for different $\delta\nu_{excite}$ values are plotted in Fig. 5d. In this non-normalized representations the electron hyperpolarization is hardly recognized. Thus, at this stage we ignore these small features, and discuss possible mechanisms leading to these effects in the SI.

In Fig. 6 E_{excite} profiles are plotted for several t_{excite} values, with $\delta\nu_{detect}$ equal to (a) 10 MHz or to (b) -30 MHz. In both cases the irradiation initially burns a narrow hole in the EPR line due to irradiation on the electron SQ transitions or the electron ^{-1}H DQ_{en} and ZQ_{en} transitions, which broadens with time. The steady state polarization distribution is reached in the timescale of the order of T_{1e} .

In Fig. 7a the experimental $E_e(\delta\nu_{excite}, t_{excite}, \delta\nu_{detect})$ values obtained at 2.7 K are shown, with $t_{excite} = 1\text{s}$. Once again, here the MW intensity was much lower ($\sim 30\text{ kHz}$) than during the measurement at 30 K. The E_{excite} profiles (Fig. 7b) again show a minima at $\delta\nu_{excite} = \delta\nu_{detect}$ and an additional broad minima closer to $\delta\nu_{excite} = 0$. Some hyperpolarization can be seen when ν_{detect} is close to zero, as indicated by the arrows in the figure, , which goes

together with a narrowing of the profile. The minima in the ZQ and DQ regions are all at about the same frequency, with large electron depolarization for large $|\delta\nu_{detect}|$ values.

The E_{detect} profiles, plotted in Fig. 7c, again show global minima around $\delta\nu_{detect} = \delta\nu_{excite}$, however here there is also a local maximum around $\delta\nu_{detect} = 0$, with lower electron polarization around it. This may indicate that electron packets which are removed in frequency are connected to one another by both eSD and another mechanism. Possible explanations for this are proposed in the supplementary information. The virtual symmetry axis of these profiles is slightly shifted with respect to the 30 K profiles, and is at about $\delta\nu_{excite} = 5$ MHz. The real magnitudes of these effects are relatively small when considering the actual measured signal, as seen in Fig. 7d.

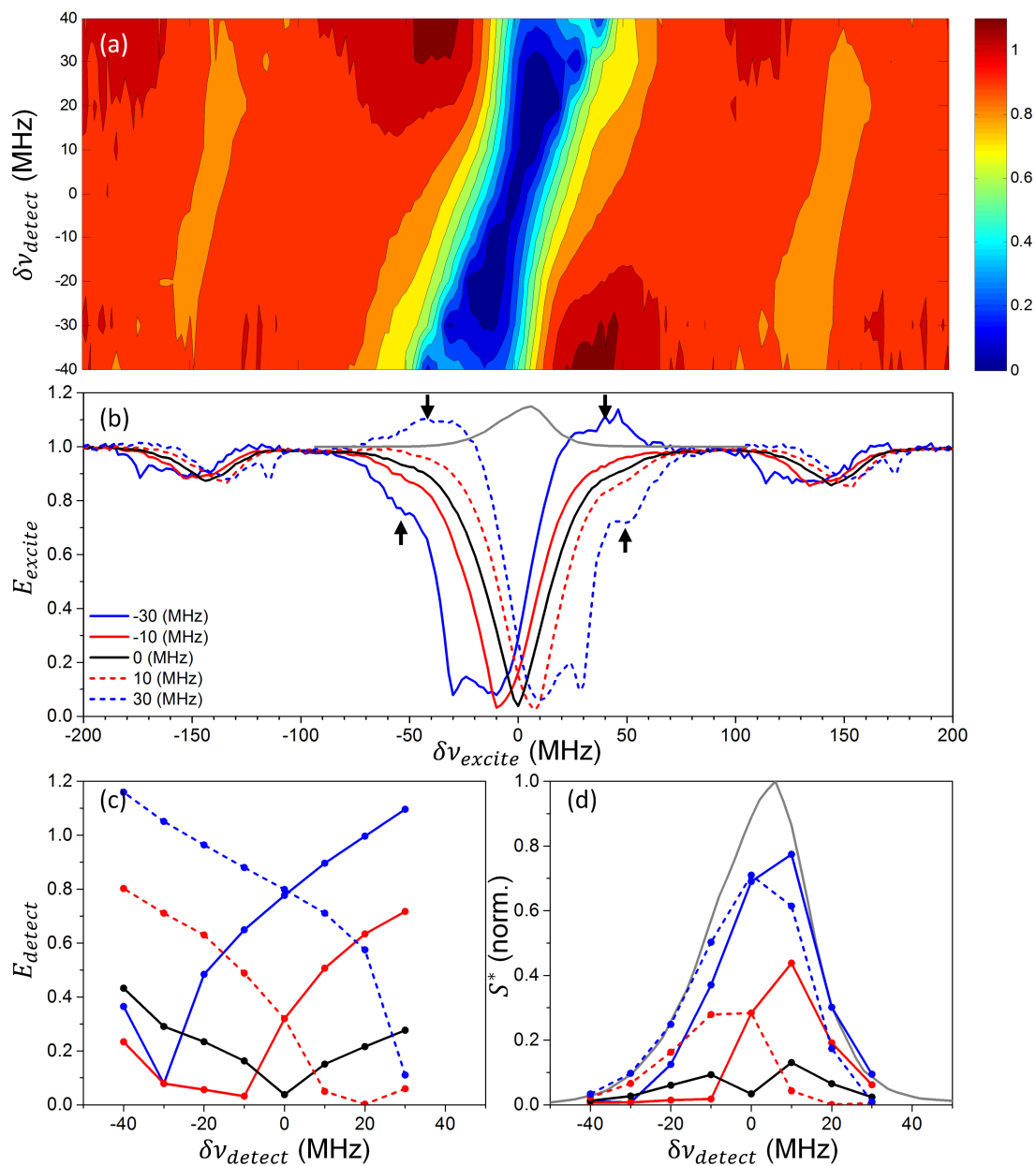


Figure 5: Measured electron saturation values as a function of $\delta\nu_{excite}$ and $\delta\nu_{detect}$ of the 15 mM trityl sample at 30 K. In (b) and (c) several E_{excite} and E_{detect} spectra are plotted, as taken from the full E_e contour shown in (a). This is done for several $\delta\nu_{detect}$ and $\delta\nu_{excite}$ values, respectively, with the values given by the color-code in (b). In (d) the expected signal intensity S^* is plotted using the values obtained from (c), as in Eq. 3. The EPR line, taken from Ref. [45], is plotted in gray in (b) and (d). The arrows in (b) show the position of the electron hyper- and de-polarization features, which are not taken into account in the simulations, as explained in the text. The measurements and simulations were obtained using $t_{excite} = 100$ ms, and a delay of 200 ms was kept between the measurements. All frequencies are given with respect to 94.86 GHz.

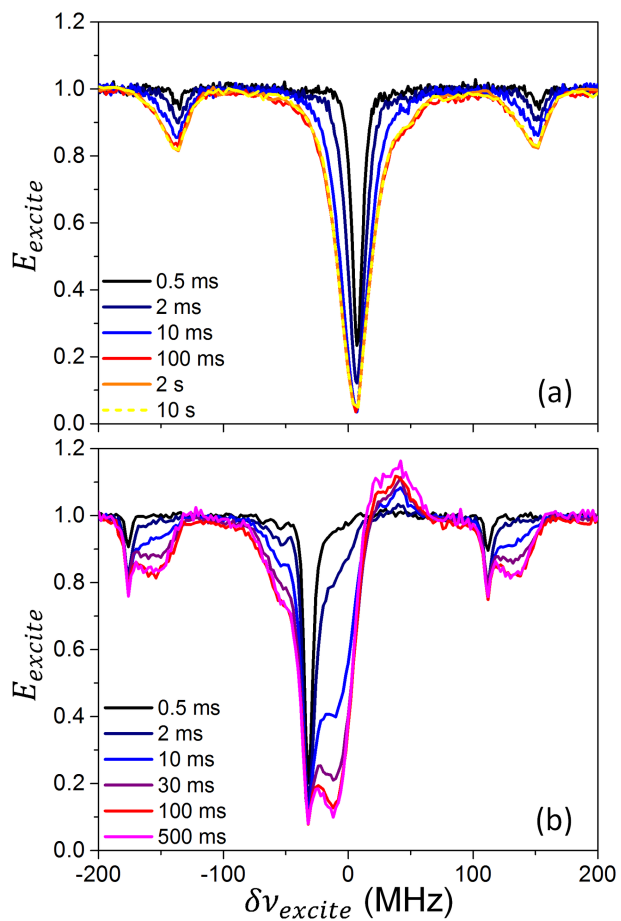


Figure 6: Measured E_{excite} spectra at different t_{excite} values of the 15 mM trityl sample at 30 K. The detection was performed at $\delta\nu_{detect}$ of (a) 10 MHz and (b) -30 MHz. All other parameters are as in Fig. 5.

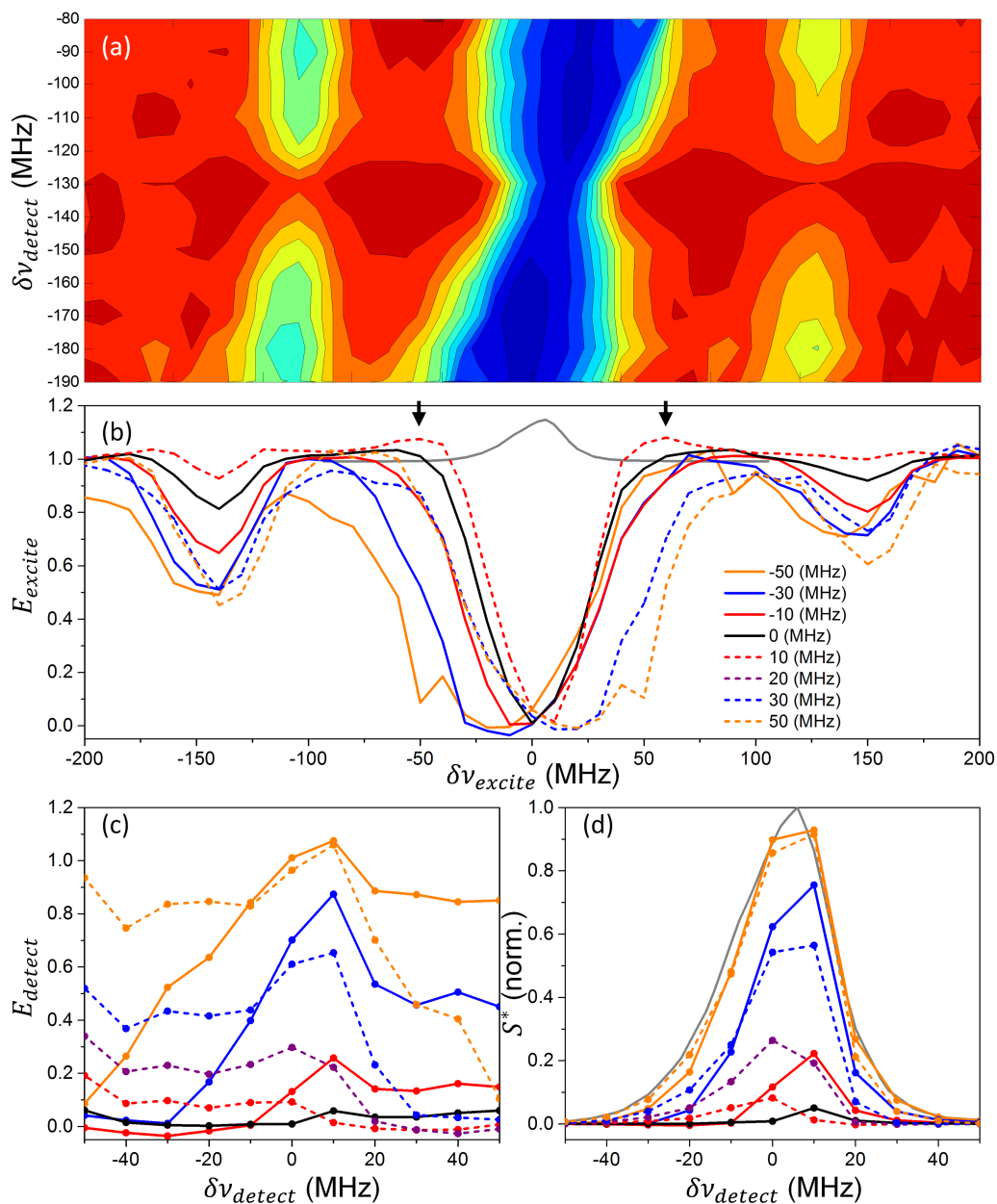


Figure 7: Measured electron saturation values as a function of $\delta\nu_{excite}$ and $\delta\nu_{detect}$ of the 15 mM trityl sample at 2.7 K. In (b) and (c) several E_{excite} and E_{detect} spectra are plotted, as taken from the full E_e contour shown in (a). This is done for several $\delta\nu_{detect}$ and $\delta\nu_{excite}$ values, respectively, with the values given by the color-code in (b). In (d) the expected signal intensity S^* is plotted using the values obtained from (c), as given in Eq. 3. The EPR line, taken from Ref. [45], is plotted in gray in (b) and (d). The arrows in (b) show the position of the electron hyperpolarization. $t_{excite} = 1$ s was used, and a delay of 1.5 s was kept between the measurements. All frequencies are given with respect to 94.86 GHz.

4 Spin temperature and the experimental results

As mentioned in the introduction, one of the fundamental assumptions of the TM mechanism is that the distribution of the electron polarizations can be described using a Zeeman temperature, T_{eZ} , associated with the weight averaged center electron frequency $\omega_{e,0}$, and an additional electron non-Zeeman spin temperature, T_{enZ} , for the parts of the Hamiltonian which contribute to the inhomogeneous EPR line shape, namely the hyperfine with strongly coupled nuclei and the g-anisotropy [64, 57, 50, 38, 35, 18, 44, 19]. The direct contribution of the dipolar interaction to T_{enZ} is assumed to be negligible. However, it plays an important indirect role as the source of the eSD process, which enables the creation of the T_{neZ} temperature in the system when its rate is faster than T_{1e}^{-1} [57, 50, 18, 19]. Under these assumptions, for long enough MW irradiation the polarization of the electrons $P_e(\omega_j)$ at a frequency $\omega_j = \omega_{e,0} + \delta\omega_{e,j}$ can be described in the ω_{MW} MW rotating frame as:

$$P_e(\omega_j, t) = -\tanh\left(\frac{\Delta\omega_e\hbar}{2k_B T_{eZ}(t)} + \frac{d\omega_{e,j}\hbar}{2k_B T_{enZ}(t)}\right), \quad (4)$$

where \hbar and k_B are the Planck and Boltzmann constants, and $\Delta\omega_e = \omega_{e,0} - \omega_{MW}$. These $P_e(\omega_j)$ values result in a monotonic change in E_{detect} , with a slope proportional to T_{enZ}^{-1} that can be positive or negative depending on the value of ω_{MW} .

We can next compare this prediction to the experimentally detected E_{detect} profiles. These profiles, obtained for the TEMPOL sample at 20 K and for the trityl sample at 30 K and 2.7 K as shown in Figs. 2c, 5c, and 7c, respectively, do not follow the expected monotonic change in $P_e(\omega_j)$. Instead they show a clear minima around $\omega_{detect} = \omega_{excite}$ and an increase of the polarizations on both sides of these conditions. In particular, the results shown in Figs. 2d, 5d, and 7d can be compared with the measurements shown in Refs. [48, 49, 50], where spin temperature was observed. The E_{excite} contours detected at 7 K and 2.7 K and plotted in Figs. 4a and 4c show only very little dependence on $\delta\nu_{detect}$, which could perhaps justify the introduction of very large T_{neZ} values. Yet in the supplementary information we show that at 7 K such a T_{enZ} does not exist. At 2.7 K further measurements are needed to verify the existence of T_{neZ} . Inspection of the ELDOR results obtained by Granwehr and Köckenberger [52] at 1.5 K leads to the same conclusion, namely that the system cannot be described by using T_{eZ} and T_{enZ} temperatures for describing the E_{detect} profiles.

5 Theoretical analysis of the ELDOR spectra

In this section we present a model for the time evolution and frequency dependence of the electron polarization that accounts for the major parts of the experimental ELDOR results.

It takes into account the effects of the spin-lattice relaxation, MW irradiation (including off-resonance effects), and eSD. In addition, the influence of the nuclei on the electrons, as was seen in the experiment, is taken into account by relying on the QM descriptions of the SE DNP processes in small spin systems [21]. A justification for relying on the spin dynamics of small model spin systems to capture the physics of large and complex spin systems can be found in Refs. [45, 46, 47]. Although the CE mechanism can have a large influence on the nuclear polarization [45, 46, 47] we did not take it into account in this model. This can be justified by the fact that during ELDOR measurements the electron polarizations do not show significant changes in timescale of the DNP enhancement buildups, and since only a small fraction of the electrons satisfy the CE condition [25, 26]. The model presented here does not rely on spin thermodynamics related parameters, such as spin temperature, energy conservation, and heat capacities of spin baths.

5.1 Theoretical model

The model presented here describes the temporal evolution of the electron and nuclear polarizations in our systems. The electron spins in these systems are assumed to have an inhomogeneous broadened spectrum due to the anisotropy of the g -tensor. As such, in the present discussion we ignore for simplicity the fact that some of the EPR features can originate from hyperfine interactions, as in the TEMPOL case. As in previous theoretical models [64, 16, 18, 51, 44, 68, 69, 70] we divide the electrons into a set of electron packets with constant average resonance frequencies, ω_j , and define an average electron polarization for each packet, $P_{e,j}$. The relative weights of the packets, f_j , are determined by normalization of the integral of the EPR line, $\sum f_j = 1$. As such, the detected EPR signal at a frequency ω_j is proportional to $N_e f_j P_{e,j}$, where N_e is the number of unpaired electrons in the system. To add the effect of the nuclei on the electrons we distinguish between two nuclear types[47]: (i) the “local” nuclei, with average polarizations $P_{n,j}$, which are directly or indirectly dipolar coupled to the electrons at ω_j , and which get polarized due to irradiation on the DQ_{en} and ZQ_{en} transitions; and (ii) the remote “bulk” nuclei, with an average polarization of P_{bulk} , which get polarized due to spin diffusion with the local nuclei. The latter determine the signals during DNP experiments.

The general form of the set of homogeneous rate equations for the electron and nuclear

polarizations, for a system with J frequency bins ($j = 1, \dots, N$) can be represented as:

$$\frac{d}{dt} \begin{bmatrix} 1 \\ P_{e,1} \\ \vdots \\ P_{e,N} \\ P_{n,1} \\ \vdots \\ P_{n,N} \\ P_{bulk} \end{bmatrix} (t) = R \begin{bmatrix} 1 \\ P_{e,1} \\ \vdots \\ P_{e,N} \\ P_{n,1} \\ \vdots \\ P_{n,N} \\ P_{bulk} \end{bmatrix} (t), \quad (5)$$

The rate matrix R in these coupled equations contains the actions of the electron (R_{1e}) and nuclear (R_{1n}) spin-lattice relaxation, the MW irradiation (R_{MW}), the nuclear spin diffusion (R_{nSD}), and the eSD (R_{eSD}) processes:

$$R = (R_{1e} + R_{1n} + R_{MW} + R_{nSD} + R_{eSD}). \quad (6)$$

The resulting polarizations can then be calculated by solving these equations for a given MW irradiation frequency ω_{excite} and time,

$$\begin{bmatrix} 1 \\ P_{e,1} \\ \vdots \\ P_{e,N} \\ P_{n,1} \\ \vdots \\ P_{n,N} \\ P_{bulk} \end{bmatrix} (\omega_{excite}, t_{excite}) = e^{R(\omega_{excite})t_{excite}} \begin{bmatrix} 1 \\ P_{e,1} \\ \vdots \\ P_{e,N} \\ P_{n,1} \\ \vdots \\ P_{n,N} \\ P_{bulk} \end{bmatrix} (0). \quad (7)$$

The explicit form of this set of equations is derived in what follows by summing up rate equations affecting one or two of these populations, derived from the rate equations for the populations in small systems, as described in Refs. [21, 22]. To transfer such rate equations on the p_α and p_β populations of a single spin $\frac{1}{2}$ to its corresponding polarization, $P = p_\beta - p_\alpha$, we use the transformation:

$$\begin{bmatrix} 1 \\ P \end{bmatrix} = \begin{bmatrix} 1 & 1 \\ -1 & 1 \end{bmatrix} \begin{bmatrix} p_\alpha \\ p_\beta \end{bmatrix}, \quad (8)$$

which conserves the total population of the system, $p_\alpha + p_\beta = 1$. In analogy, the populations

of an electron-nuclear two-spin system, p_{α_e, α_n} , p_{α_e, β_n} , p_{β_e, α_n} , p_{β_e, β_n} , (assuming a nucleus with spin $\frac{1}{2}$) can be transferred to the $P_e = -p_{\alpha_e, \alpha_n} - p_{\alpha_e, \beta_n} + p_{\beta_e, \alpha_n} + p_{\beta_e, \beta_n}$ and $P_n = p_{\alpha_e, \alpha_n} - p_{\alpha_e, \beta_n} + p_{\beta_e, \alpha_n} - p_{\beta_e, \beta_n}$ polarizations, the difference polarization $P_{en} = p_{\alpha_e, \alpha_n} - p_{\alpha_e, \beta_n} - p_{\beta_e, \alpha_n} + p_{\beta_e, \beta_n}$ and the conserved sum polarization $1 = p_{\alpha_e, \alpha_n} + p_{\alpha_e, \beta_n} + p_{\beta_e, \alpha_n} + p_{\beta_e, \beta_n}$:

$$\begin{bmatrix} 1 \\ P_e \\ P_n \\ P_{en} \end{bmatrix} = \begin{bmatrix} 1 & 1 & 1 & 1 \\ -1 & -1 & +1 & +1 \\ 1 & -1 & 1 & -1 \\ 1 & -1 & -1 & 1 \end{bmatrix} \begin{bmatrix} p_{\alpha_e \alpha_n} \\ p_{\alpha_e \beta_n} \\ p_{\beta_e \alpha_n} \\ p_{\beta_e \beta_n} \end{bmatrix}. \quad (9)$$

Here we have neglected the effect of the small state mixing that is present in a electron-nuclear system due to the non-secular hyperfine interaction. This effect is compensated for by the introduction of the effective DQ_{en} and ZQ_{en} irradiation derived from the MW irradiation in the case of the SE. The transformation results in two time independent polarization components 1 and P_{en} and the latter can therefore be neglected. This approach is obviously a simplified version of the calculations of the quantum dynamics in a many-spin systems[21, 71, 23, 25, 26].

5.1.1 The spin-lattice relaxation rates

The electron spin-lattice relaxation rate matrix is given by $R_{1,e} = \sum R_{1,e}^j$, where $R_{1,e}^j$ are matrices with non zero-elements of the form $T_{1e,j}^{-1} \begin{bmatrix} 0 & 0 \\ P_{e,j}^0 & -1 \end{bmatrix}$ in the $\begin{bmatrix} 1 \\ P_{e,j} \end{bmatrix}$ subspace [72, 73], where $P_{e,j}^0 = -\tanh(\omega_{e,j}\hbar/2k_B T_l)$ are the thermal equilibrium polarizations of the electrons, and T_l is the lattice temperature. In analogy, the nuclear spin-lattice rate matrix of the nuclei is defined as $R_{1,n} = \sum R_{1n,j} + R_{1bulk}$, where $R_{1n,j}$ are the non-zero elements given by $T_{1n,j}^{-1} \begin{bmatrix} 0 & 0 \\ P_n^0 & -1 \end{bmatrix}$ in the $\begin{bmatrix} 1 \\ P_{n,j} \end{bmatrix}$ subspace, and the bulk relaxation rate matrix R_{1bulk} has the form $T_{1,bulk}^{-1} \begin{bmatrix} 0 & 0 \\ P_n^0 & -1 \end{bmatrix}$ in the $\begin{bmatrix} 1 \\ P_{bulk} \end{bmatrix}$ subspace. The equilibrium polarization of the nuclei equals $P_n^0 = \tanh(\omega_n\hbar/2k_B T_l)$, where ω_n is the magnitude of the nuclear Larmor frequency, and for simplicity we assume that the nuclei have the same sign of the gyromagnetic ratio as for ^1H nuclei.

In the present model we do not consider explicitly electron-nuclear cross-relaxation processes. We realize however that during calculations the effects of cross relaxation processes can in many instances be mimicked by combining electron and nuclear relaxation processes[21].

5.1.2 The MW irradiation

The MW irradiation field, of strength ω_1 and applied at a frequency ω_{excite} , can excite in our model the SQ transitions, the DQ_{en}, and the ZQ_{en} transitions. To make a distinction between the three types of contributions to the relaxation matrix R_{MW} representing the MW irradiation effect we write:

$$R_{MW} = \sum R_{SQ}^j + \sum R_{DQ}^j + \sum R_{ZQ}^j. \quad (10)$$

The R_{SQ}^j matrices have a single diagonal element operating on $P_{e,j}$ with a value

$$w_j^{SQ} = -\frac{(\omega_1)^2 T_{2e}}{1 + \Delta\omega_j^2 T_{2e}^2}, \quad (11)$$

where T_{2e} is the electron spin-spin relaxation time of the system (rather than the phase memory time measured in time domain EPR) and $\Delta\omega_j = \omega_{e,j} - \omega_{excite}$ is the off resonance value of the electron packet at ω_j . The expressions for these rates rely on the assumption that $|\omega_1| \ll |T_{2e}^{-1} + i\Delta\omega|$ [21, 22]. When this does not hold this will result in a saturation time constant that is larger than T_{2e} .

The MW irradiation on the DQ_{en} or ZQ_{en} transitions of an electron coupled to neighboring nuclei becomes allowed due to the state mixing induced by the pseudo-secular parts of their hyperfine interactions. This irradiation results in a SE process polarizing the nuclei and is represented by the matrix elements of $R_{ZQ/DQ}^j$. This DQ_{en} or ZQ_{en} irradiation results in an equilibration of the polarizations of the electron and the nuclei [21]. If on average an electron in bin j transfers its polarization to η nuclei, and assuming the polarizations of these nuclei become all equal due to fast spin diffusion rates or dipolar state mixing, the MW irradiation will result in the ideal case in a steady state polarization of the electron given by $P_{e,j} = \pm P_{n,j} = P_{e,j}^0/(\eta + 1)$. To accomplish this, the sub-matrices R_{DQ}^j and R_{ZQ}^j in the subspace $\begin{bmatrix} P_{e,j} \\ P_{n,j} \end{bmatrix}$ have the general form $\frac{1}{2}w_{DQ}^j \begin{bmatrix} -1 & 1 \\ \eta^{-1} & -\eta^{-1} \end{bmatrix}$ and $\frac{1}{2}w_{ZQ}^j \begin{bmatrix} -1 & -1 \\ -\eta^{-1} & -\eta^{-1} \end{bmatrix}$, respectively. The actual steady state polarization of the electrons and nuclei during the MW irradiation will be influenced not only by the action of these DQ and ZQ effective irradiation, but also by the relaxation times of the system[21]. The values of the $w_{DQ/ZQ}^j$ rates can be estimated using perturbation theory on the Bloch equations[21, 22] as

$$w_j^{DQ/ZQ} = \frac{(\frac{\bar{A}^\pm}{2\omega_n}\omega_1)^2 T_{2,e}}{1 + (\omega_{excite} - (\omega_{e,j} \mp \omega_n))^2 T_{2,e}^2}, \quad (12)$$

where \bar{A}^\pm is some effective hyperfine coefficient that corresponds to the average root mean square sum of the pseudo-secular hyperfine term of the nuclei polarized by each electron.

Although here the bulk nuclei are polarized *via* the local nuclei (*i.e.* their hyperfine interaction value is taken to be zero), it is possible to conduct the simulations by considering both of these nuclei together. This is justified for fast spin diffusion rates. In such a case only the bulk polarization should be taken into account in Eq. 5, and $R_{DQ/ZQ}$ in Eq. 10 should be substituted by $R_{DQ/ZQ}^{bulk} = \sum R_{DQ/ZQ}^{j,bulk}$ with rate matrices $R_{DQ/ZQ}^{j,bulk}$ with elements $\frac{1}{2}w_{DQ}^{j,bulk} \begin{bmatrix} -1 & 1 \\ (\eta_j^b)^{-1} & -(\eta_j^b)^{-1} \end{bmatrix}$ and $\frac{1}{2}w_{ZQ}^{j,bulk} \begin{bmatrix} -1 & -1 \\ -(\eta_j^b)^{-1} & -(\eta_j^b)^{-1} \end{bmatrix}$ in the subspace $\begin{bmatrix} P_{e,j} \\ P_{bulk} \end{bmatrix}$. The expressions for $w_{DQ/ZQ}^{j,bulk}$ are the same as in Eq. 12 by replacing \bar{A}^\pm by an effective bulk hyperfine coefficient A_{bulk}^\pm . The η_j^b parameter must be adjusted to the average number of polarized bulk nuclei per electron, which can be defined by $\eta_j^b = C_n/f_{e,j}C_e$, where C_e and C_n are the concentrations of the electrons and nuclei, respectively, and $f_{e,j}C_e$ is the concentration of the electrons with a frequency ω_j . Once again, here we will consider the bulk nuclei to be polarized *via* spin diffusion by the local nuclei, as explained in what follows.

5.1.3 Spin Diffusion

The spin diffusion process, which transfers polarization between the local and bulk nuclei, is introduced using a rate matrix R_{nSD} . This matrix is given by $R_{nSD} = \sum R_{nSD}^j$, with R_{nSD}^j having non-zero elements $w^{nSD} \begin{bmatrix} -1 & 1 \\ \eta/\eta_j^b & -\eta/\eta_j^b \end{bmatrix}$ in the $\begin{bmatrix} P_{n,j} \\ P_{bulk} \end{bmatrix}$ subspace [74, 47], where w^{nSD} is the effective nuclear spin diffusion rate between neighboring nuclei and η_j^b/η is the ratio between the bulk and local nuclei.

5.1.4 Spectral Diffusion

Finally, the spectral diffusion rate matrix R_{eSD} must be added to the rate equations. Deriving the general form of this matrix, we make the following assumptions: (i) The eSD process can be described by introducing effective (single) rate constants defining the polarization transfer process between pairs of bins. (ii) At thermal equilibrium the polarizations satisfy the Boltzmann distribution $\epsilon_{j,j'} = \frac{P_{e,j}^0}{P_{e,j}^0}$. And (iii), the eSD process conserves the total polarization of the electron spin system, $\frac{d}{dt}(N_e \sum f_j P_j) = 0$. As a result our eSD model is not energy conserving, as is required in the spectral diffusion process considered in the theory leading to the TM mechanism [75]. Based on these assumptions, the polarization exchange process described by the R_{eSD} matrix can be expressed as a sum of $R_{j,j'}^{eSD}$ rate matrices ,

$R_{eSD} = \sum_{j,j'} R_{j,j'}^{eSD}$, which have non-zero elements of the form

$$\overline{w}_{j,j'}^{eSD} \frac{1}{\epsilon_{j,j'} + 1} \begin{bmatrix} -\epsilon_{j,j'} f_{j'} & f_{j'} \\ \epsilon_{j,j'} f_j & -f_j \end{bmatrix} \quad (13)$$

in the $\begin{bmatrix} P_{e,j} \\ P_{e,j'} \end{bmatrix}$ subspace. For the $\overline{w}_{j,j'}^{eSD}$ polarization exchange rate, and in particular its dependence on the frequency difference between the bins, we choose the form:

$$\overline{w}_{j,j'}^{eSD} = \frac{\Lambda^{eSD}}{(\omega_j - \omega_{j'})^2}, \quad (14)$$

where Λ^{eSD} is a fitting parameter. A justification for expressing the rates in this form is given in appendix A. As will be shown in the next sections, this form enabled us to analyze all detected ELDOR spectra, indicating the validity of this $(\omega_j - \omega_{j'})$ dependence.

In order to characterize the effect of the R_{eSD} rate matrix we can define a characteristic polarization exchange rate constant by considering the exchange rate between the polarizations of the electrons in neighboring bins j_{max} and j_{max-1} with the largest f_j values, f_{max} and f_{max-1} :

$$(T_{max}^{eSD})^{-1} = \frac{1}{2} \overline{w}_{j_{max},j_{max-1}}^{eSD} (f_{max} + f_{max-1}) = \frac{\Lambda^{eSD} (f_{max} + f_{max-1})}{2(\omega_{j_{max}} - \omega_{j_{max-1}})^2}. \quad (15)$$

5.2 Simulations of the experimental data

In order to compare the simulations with the experimental results, the electron polarizations were calculated using Eq. 7, with the initial values of the polarization set to their thermal values for the electrons and set to zero for the nuclei, where the latter mimics the effect of ideal saturation of the nuclei. The simulated saturation values of the different electrons can then be obtained using

$$E_e(\omega_{excite}, t_{excite}, \omega_j) = P_{e,j}(\omega_{excite}, t_{excite}) / P_{e,j}(0), \quad (16)$$

in analogy to Eq. 2 with $\omega_{detect} = \omega_j$. The E_{excite} and E_{detect} profiles are defined, in analogy to the experimental profiles, as the $E_{e,j}$ value of the single electron packet at $\omega_j = \omega_{detect}$ as a function of the excitation frequency ω_{excite} , and as the $E_{e,j}$ profile of the different electron packets obtained using a single ω_{excite} value, respectively, and for a given t_{excite} value. The simulated profiles were compared with experimental E_e profiles, and the fitted values were determined using a visual fitting procedure, by varying the parameters defining the matrix

elements of the rate matrix in Eq. 7. In addition, the expected EPR signal can be calculated using

$$S^*(\omega_j; \omega_{excite}, t_{excite}) = f_j \cdot E_e(\omega_{excite}, t_{excite}, \omega_j), 17 \quad (17)$$

in analogy with Eq. 3.

The parameters entering the total rate matrix can be divided into two groups: those that are experimentally determined - i.e. the T_{1e} and $T_{1n,bulk}$ relaxation times, the values of f_j , the MW irradiation strength ω_1 and the concentrations of the electrons and bulk nuclei, C_e and C_n ; and those that we cannot determine experimentally are chosen to fit the experimental results - i.e. the T_{2e} relaxation time (which is longer than the phase memory time of the system), the \bar{A}^\pm value, the w^{nSD} rate and the Λ^{eSD} coefficient, the $T_{1n,j}$ relaxation time of the local nuclei, and their concentration ηC_e . In addition, we must choose the width of the frequency bins, $\omega_j - \omega_{j-1}$. These parameters depend on one another, and in particular on bin size, which changes the frequency range on which the averaging is performed. As there are many unknown parameters the fit to the data was done manually and the parameter set chosen is not necessarily the only possibility to fit the data. The significance of the parameter values used in our simulations, as summarized in Table 2, is then in their consistency for different experimental conditions, rather than in their absolute value. In order to simplify the problem, a single $T_{1e,j}$ time was used for all j and was set equal to the experimental T_{1e} value, the T_{2e} value used was not changed with temperature, and ω_1 was assumed to be frequency independent. A bin width of $(\omega_j - \omega_{j-1})/2\pi = 2$ MHz was used due to computation limitations when considering the TEMPOL sample, and was kept the same in the case of the trityl sample for comparison, although in the latter a smaller value could be used.

The fitting of the experimental data was performed based on the E_{excite} profiles in two steps. At first only the electron system was considered, by removing the $R_{DQ/ZQ}$ irradiation matrices (Eq. 10) and by varying ω_{excite} only in the frequency range of the EPR line. The shape of the simulated ELDOR spectrum then depends on the T_{2e} and Λ^{eSD} fitting parameters, with the former influencing the MW saturation efficiency as given in Eq. 11. For the TEMPOL sample, where the MW irradiation can directly saturate only a small fraction of the EPR line and the spectral diffusion was dominant for the given experimental conditions, T_{2e} had a relatively small effect on the ELDOR profile. The measured ELDOR spectra were then fitted by varying the Λ^{eSD} rate and using $T_{2e} = 10 \mu s$, which is a reasonable guess. A ten-fold increase in T_{2e} had a negligible effect and a small effect could be seen for a twofold change of the bin width. In the trityl sample the direct MW excitation can have a large influence on the entire EPR line, and a longer value of $T_{2e} = 100 \mu s$ had to be used to reduce this effect and allow for the experimental ELDOR profiles to be fitted. Λ^{eSD} was then found for this particular choice of T_{2e} and bin width.

In the second step the $R_{DQ/ZQ}$ rates were reintroduced. In the trityl case, where the EPR line is much narrower than the ^1H Larmor frequency, this step only affects the ELDOR results for irradiation outside of the EPR line, and therefore has no effect on the results of the first step within physical limits. In the TEMPOL case the MW irradiation can excite SQ, DQ and ZQ transitions simultaneously. However, for the parameters used in the first step, the $R_{DQ/ZQ}$ rates had little influence on the ELDOR profiles for ν_{excite} within the EPR line. This may not be the case when the influence of the spectral diffusion is reduced. Therefore, in both cases the main influence of these rates was for the case of irradiation outside of the EPR line. The ELDOR spectrum in this region was then influenced \bar{A}^\pm , η , w^{nSD} , and the T_{1n} parameters, as well as on the T_{2e} and Λ^{eSD} parameters. The latter two were chosen based on the values used in the first step. The ELDOR profiles were hardly influenced by the loss of polarization to the local nuclei and was strongly influenced by the polarization transfer to the bulk nuclei. As such $T_{1n,j}$ were chosen to be equal to the experimentally measured $T_{1,bulk}$. The value of w^{nSD} was chosen to be of the order of the nuclear dipolar interaction, 1000 s^{-1} , resulting in strong coupling between the local and bulk nuclei. The polarization transfer between the electrons to the bulk nuclei then depended on \bar{A}^\pm and η parameters, with a faster polarization transfer for larger values of the two. Here the experimental ELDOR spectra were fitted by varying the \bar{A}^\pm while using $\eta = 4$ as a reasonable guess.

Radical	TEMPOL	Trityl
$\omega_{1H}/2\pi$ (MHz)	144	
$\omega_e/2\pi$ (GHz)	~ 95	
^1H concentration (M)	100	
Radical concentration (M)	0.04	0.015
$(\omega_j - \omega_{j-1})/2\pi$ (MHz)	2	
T_{2e} (μs)	10	100
Λ^{eSD} (μs^{-3})	2000	10
w^{nSD} (μs^{-1})	0.001	
A^\pm (MHz)	10	0.1
$\omega_1^*/2\pi$ (MHz)	0.6	

Table 2: Parameter values used in the simulation of the E_e profiles. The values of T_{1e} and T_{1n} were taken from Table 1.

* $\omega_1/2\pi = 0.03 \text{ MHz}$ was used at 2.7 K

5.2.1 TEMPOL sample

In order to fit the experimental data shown in Figs. 2-4 the TEMPOL EPR line-shape shown in Ref. [45] (gray line in Fig 8b,d) was used. The ^{14}N nuclei of TEMPOL have a large influence on this line-shape, through their hyperfine interactions, and their relaxation may

have a significant effect on the ELDOR line-shapes[76, 52, 77, 78]. However, for simplicity their presence was not taken explicitly into account in the simulations, except for their influence on the EPR line-shape itself. The results of these simulations for the measurements at 20 K are shown in Figs. 8 and 9, and Fig. 10 for 7K and 2.7 K. The parameters used in these simulations are summarized in Table 2. The fits were obtained using an eSD rate constant $\Lambda^{eSD} = 2000 (\mu\text{s})^{-3}$, resulting in a characteristic T_{max}^{eSD} time of about 10 μs (with $f_{max} + f_{max-1} = 0.017$ in Eq. 15). This rate is much faster than T_{1e}^{-1} , even at 20 K, and therefore has a significant influence on the electron polarization distribution.

Starting with the data obtained at 20 K it can be seen that a good agreement is obtained between the experimental and simulated results, with the simulations showing all main features of the E_{excite} and E_{detect} profiles (as well as the corresponding S^* profiles). This includes both the effects of direct irradiation on the detected electrons close to $\delta\nu_{detect} = \delta\nu_{excite}$, the polarization spread due to the eSD mechanism, and the effect of irradiation on the DQ_{en} and ZQ_{en} transitions. There are however some differences that will be discussed now.

First, the temporal dependence of the experimental E_{excite} profiles shows some narrowing of its shape at relatively long times. This is not fully reproduced by the simulations. The source of this effect can be due to an oversimplification of the nuclear saturation process, or due to the presence of the ^{14}N nuclear relaxation that was not taken into account in the rate equations. In addition, the polarizations at $\delta\nu_{detect} = \delta\nu_{excite}$ is lower in the simulation than observed experimentally. This is a result of an over estimation of the SQ MW representation in Eq. 11, in particular since a single off resonance value is used for all electrons in each bin. These differences could have been corrected by applying a simple convolution procedure on the simulated profiles, mimicking the action of the detection sequence. This was not done in order to demonstrate the sharp saturation features resulting from this model. An average off resonance value could also have been added to the calculation to reduce these differences, which would also have resulted in an increase of the \bar{A}^{\pm} value needed in order to fit the experimental results.

The ELDOR data recorded at 7 K and 2.7 K are again in good agreement with the simulated results. In particular, it is apparent that the broadening of the E_{excite} ELDOR profiles is a consequence of the lengthening of T_{1e} . The simulated spectra reach values that are somewhat lower than the experimental ones, and which could be a result of the finite baseline artifact, b , as described around Eq. 2. The influence of the nuclei on the ELDOR data manifests itself in the form of sharp features that are more pronounced in the simulated profiles than in the experimental one. Possible changes in the EPR line-shape at low temperatures are not investigated and are left for future studies, together with the

influence of the instantaneous and eSD on the spin relaxation measurements. It should be noted that some mismatches between the simulations and the experiments at different temperatures can be reduced when the individual ELDOR spectra are fitted independently. In addition, the influence of the nuclei on the ELDOR data could also have been calculated by considering both the local and bulk nuclei together, as explained in section 5.1.2.

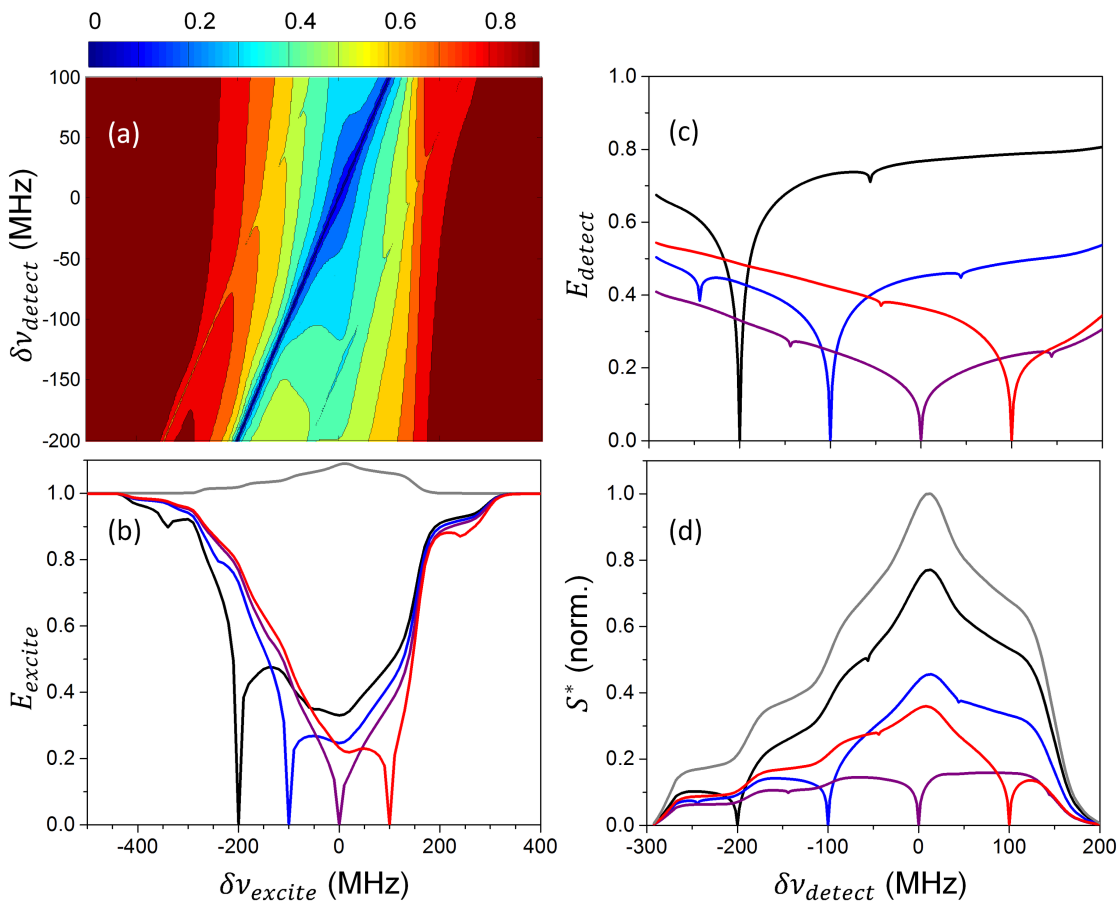


Figure 8: Normalized electron polarizations $E_e(\delta\nu_{excite}, t_{excite}, \delta\nu_{detect})$ simulated for the 40 mM TEMPOL sample at 20 K for a set of excitation and detection frequencies $\nu_{excite} = \nu_0 + \delta\nu_{excite}$ and $\nu_{detect} = \nu_0 + \delta\nu_{detect}$, with $\nu_0 = 95$ GHz, and using $t_{excite} = 10$ ms. In (a) the simulated data are presented in a contour plot and in (b) and (c) individual $E_{excite}(\delta\nu_{excite})$ and $E_{detect}(\delta\nu_{detect})$ profiles are shown. In (b) the colors of the different profiles correspond to constant $\delta\nu_{detect}$ values that are assigned inside the figure. In (c) the colors of the profiles correspond to constant $\delta\nu_{excite}$ values using the same color codes as defined inside (b). The top spectrum in (b) is the EPR spectrum taken from Ref. [45]. In (d) the expected EPR signal intensity $S^*(\delta\nu_{detect}; \delta\nu_{excite}, t_{excite})$ is plotted as a function of $\delta\nu_{detect}$, for different $\delta\nu_{excite}$ values, derived from the EPR line-shape (gray line) and the profiles in (c), as given by Eq. 3. The parameters used in the simulations are given in Table 2.

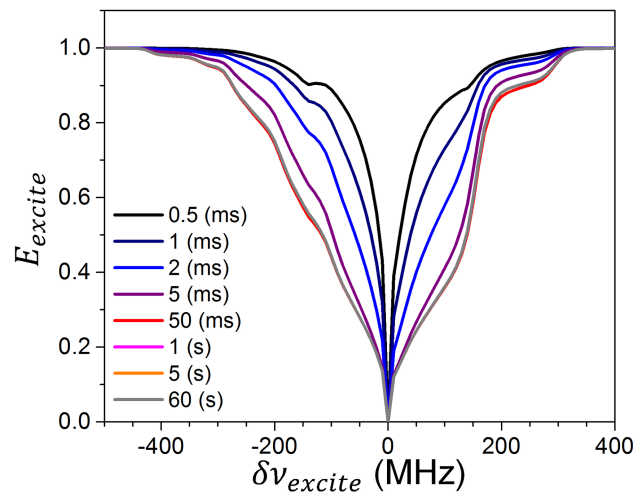


Figure 9: Simulated $E_{excite}(\delta\nu_{excite})$ spectra for different t_{excite} values of the 40 mM TEMPOL sample at 20 K with $\nu_{excite} = \nu_0 + \delta\nu_{excite}$, $\nu_0 = 95$ GHz, and using a detection frequency of $\nu_{detect} = 95$ GHz ($\delta\nu_{detect} = 0$). The t_{excite} values are defined by the color coding inside the figure. The parameters used in the simulations are given in Table 2.

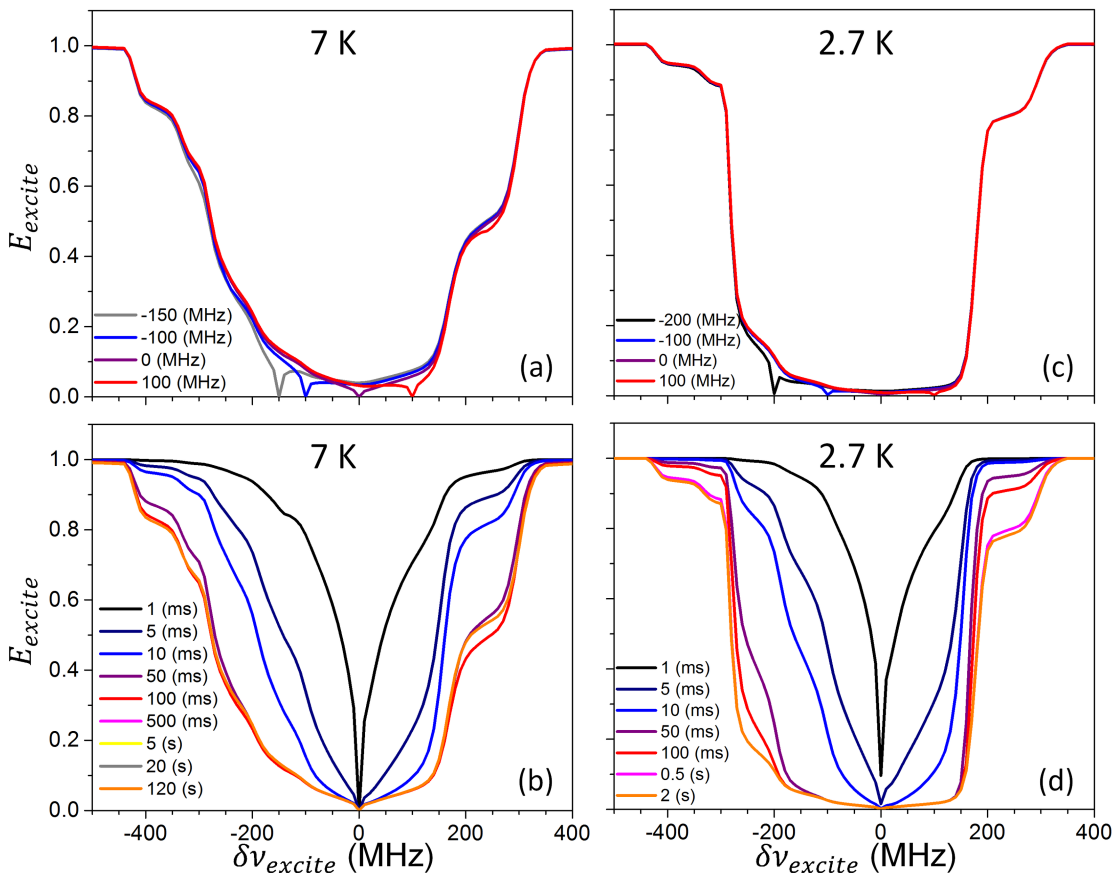


Figure 10: Normalized electron polarizations $E_e(\delta\nu_{excite}, t_{excite}, \delta\nu_{detect})$ simulated for the 40 mM TEMPOL sample at 7 K and 2.7 K. These were done for a set of excitation and detection frequencies $\nu_{excite} = \nu_0 + \delta\nu_{excite}$ and $\nu_{detect} = \nu_0 + \delta\nu_{detect}$, with $\nu_0 = 95$ GHz. In (a) $E_{excite}(\delta\nu_{excite})$ profiles at 7 K are plotted for several $\delta\nu_{detect}$ values, defined by the color coding inside the figure, and using $t_{excite} = 100$ ms. In (b) $E_{excite}(\delta\nu_{excite})$ profiles at 7 K are plotted using for increasing t_{excite} values, defined by the color coding inside the figure, with $\delta\nu_{detect} = 0$. In (c) and (d) similar profiles are plotted as in (a) and (b) but at 2.7K, with $\omega_1/2\pi = 30$ kHz in stead of 600 kHz, and using $t_{excite} = 500$ ms in (c). The parameters used in the simulations are given in Table 2.

5.2.2 Trityl sample

The experimental profiles in Figs. 5 and 6 can also be analyzed by simulating similar saturation profiles using the coupled rate equations in Eq. 5. Relying on the EPR line-shape reported in Ref. [46], the simulated profiles are shown in Figs. 11 and 12, where we used the parameters summarized in Table 2. Once again, a relatively short $T_{2,e}$ value had to be used during these simulations in order to reduce the electron depolarization originating from off resonance irradiation on the SQ transitions. The fitted value of Λ^{eSD} results in a characteristic T_{max}^{eSD} time of about 250 μ s (with $f_{max} + f_{max-1} = 0.125$ in Eq. 15), which is

again much faster than T_{1e} .

The shapes of the simulated E_{excite} profiles, as plotted in Fig. 11b, show many of the experimental features, but do not capture exactly the change in the position of the broad minima. As expected, the extra depolarization and hyperpolarization effects are not reproduced, because the source of these effects is not present in our rate equations. The individual simulated E_{detect} shapes in 11c have the same general features as in the experiment, with a minima around $\delta\nu_{excite} = \delta\nu_{detect}$ with a larger recovery towards the thermal value for irradiation farther away from $\delta\nu_{excite} = 0$. However, the experimental E_{detect} curves obtained for high $|\delta\nu_{excite}|$ values are less symmetrical with respect to $\delta\nu_{excite} = \delta\nu_{detect}$ than the simulated ones. These differences are much less pronounced when comparing the total electron polarization at each frequency bin derived from $S_j^* = f_j P_{e,j}(\delta\nu_{excite}, t_{excite})$, as shown in Fig. 11d. The simulated time dependence of the E_{excite} profiles (Fig. 12), showing the gradual change from a narrow hole in the electron polarization to broad eSD mediated features, are in agreement with the experimental results.

Some specific features appearing in 2.7 K measurements (Fig. 7) cannot be captured using our present model, and we therefore leave their interpretation for a later study. Whether or not their appearance are correlated with the unique extra features observed at 30 K must still be studied. Possible sources for these observations are large dipolar or hyperfine interactions, which cause large splittings in the SQ spectra of electrons such that only one transition can be detected[79]. This is illustrated in the supporting information, based on QM calculations performed on small model spin systems.

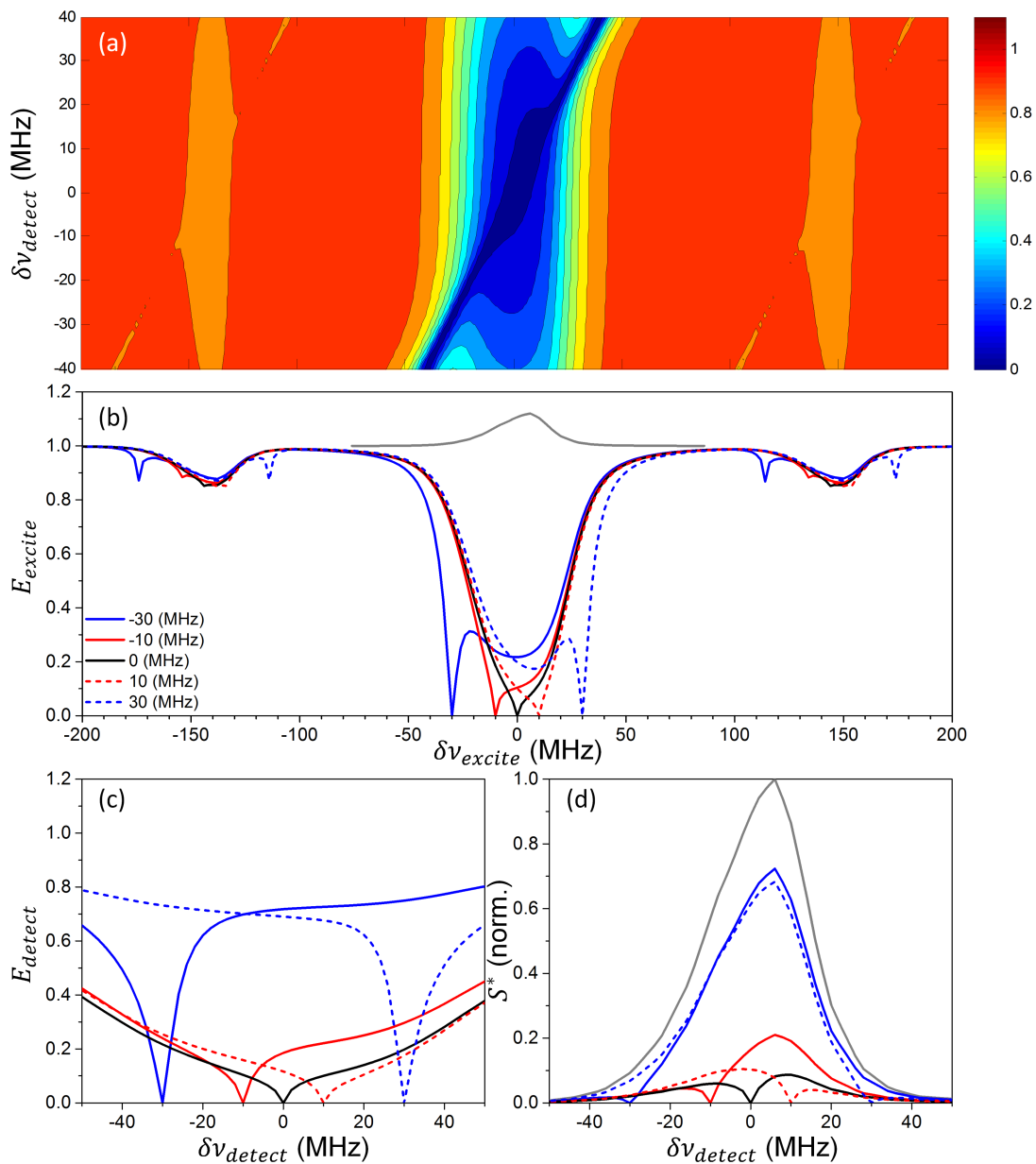


Figure 11: Simulated E_e as a function of ν_{excite} and ν_{detect} , using the parameters of the 15 mM trityl sample at 30 K, as given in Table 2, and using $t_{excite} = 0.1$ s. Several individual E_e spectra are plotted *vs.* $\delta\nu_{excite}$ in (b) and (c), and *vs.* $\delta\nu_{detect}$, using $\delta\nu_{detect}$ and $\delta\nu_{excite}$ values as given in (b). In (d) the expected signal intensity S^* is plotted using the values obtained from (c). The EPR line used in the simulations, which was taken from Ref. [46], is plotted in gray in (b) and (d). A reference frequency of 94.86 GHz was used in all cases.

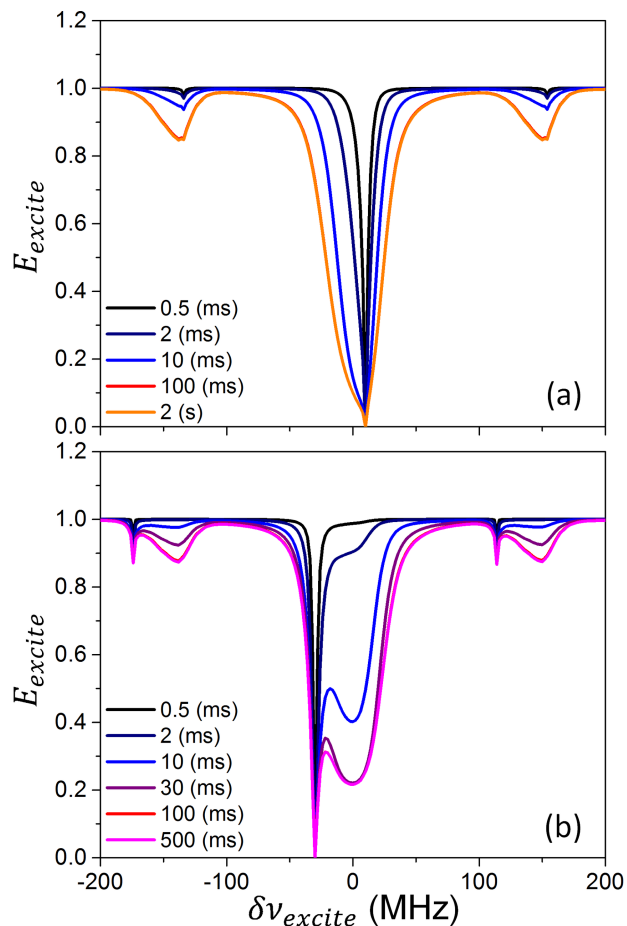


Figure 12: Simulated E_e as a function of $\delta\nu_{excite}$ for several t_{excite} values, using the parameters of the 15 mM trityl sample at 30 K, and with $\delta\nu_{detect}$ of (a) 10 MHz and (b) -30 MHz. All other parameters are as in Fig. 11.

6 Discussion

In this study we have focused on the electron depolarization during static ELDOR experiments in the solid state. From the ELDOR data it immediately follows that for both the trityl sample, at 30 K and 2.7 K, and the TEMPOL sample, at 20, 7, and 2.7 K, the electron polarization is highly affected by the electron spectral diffusion (eSD) process. The ELDOR results were used to monitor the polarization of the electrons during MW irradiation at a fixed frequency, offering a way to infer whether a spin temperature was created in the electron non-Zeeman manifold, in analogy to the cw EPR detected results shown in Refs. [48, 49, 50]. Although an energy conserving eSD mechanism was postulated to lead to the creation of such a temperature, our measurements on the TEMPOL sample at 20 K (and

the 7 K results to a lesser extent) and the trityl containing sample at 30 and 2.7 K, show clearly that the distribution of the electron polarization cannot be described using the two spin temperatures coefficients appearing in Eq. 4. We conclude that the TM mechanism, as described by the Provotorov based high temperature rate equations or the low temperature Borghini based model [64, 50, 35, 18, 44], can not be used to analyze DNP data under the conditions used here. However, these results do not show whether a common dipolar temperature[50] exists in our samples, and does not directly contradict the assumptions of the bin-based TM models presented in Refs. [51, 68, 69, 70].

The experimental results presented here differ from those of Granwehr and Köckenberger [52], where the double minima in the ELDOR spectra was not observed. This may be due to the difference in samples, measurement conditions, or detection schemes has to be addressed elsewhere. However, in both cases the eSD has a large influence on the electron polarization. Analyzing their results in the same manner as in section 4 does again not show the formation of the above mentioned spin temperatures.

The theoretical model describing the electron depolarization presented here captures almost all of the experimental ELDOR features in the TEMPOL and the trityl case, and especially the main features due to the eSD mechanism in the TEMPOL sample. This can next be used to study the effects of the eSD on the shapes of DNP spectra, which will enable us to improve the SE and CE based analysis used in Refs. [45, 46, 47] and our understanding of the electron and nuclear spin dynamics during MW irradiation. In particular, the electron depolarization is expected to result in a reduction of the DNP efficiency [21, 55], which can lead to a change in the expected SE and CE line-shapes and may explain the decrease of the DNP efficiency at low temperatures reported earlier[45, 46, 47].

The eSD rates used here do not depend on temperature, and resulted in Λ^{eSD} and T^{eSD} parameters of $10 (\mu\text{s})^{-3}$ and $250 \mu\text{s}$ for the trityl sample and $2000 (\mu\text{s})^{-3}$ and $10 \mu\text{s}$ for the TEMPOL sample (as defined in Eq. 15). As the magnitude of Λ^{eSD} is expected to scale with the cube of the average dipolar interaction (see appendix A), it can be expected that Λ^{eSD} for 15 mM trityl will be about an order of magnitude smaller than for 40 mM TEMPOL. That the actual ratio is still another order of magnitude smaller can be attributed to model limitations or to physical differences between the radicals. The former includes effects of the finite bin size and uncertainty in the simulation parameters - such as the value of T_{2e} . Physical reasons include non-eSD electron polarization transfer mechanisms, such as polarization transfer to the nuclei and electron-nucleus relaxation, and in particular to the ^{14}N nuclei in the TEMPOL sample[76, 52, 77, 78]. Such non-eSD mechanisms can explain the narrowing of the E_{excite} profile of the TEMPOL sample at long MW irradiation times (Figs. 3 and 4). As a result of this discussion we must conclude that at this point the fitted values

of Λ^{eSD} cannot yet be straightforwardly correlated to network of interacting electrons and the fluctuating dipolar interactions between them. More experimental results are necessary to enable us to interpret the Λ^{eSD} values and to investigate their temperature dependence. These experiments must include measurements at different electron concentrations on each of the radical types and replacing ^1H nuclei by ^2H , and in nitroxide based radicals ^{14}N by ^{15}N . In addition, a better knowledge of the mechanism can be gained by measuring the electron polarization distribution as a function of time.

To conclude, in this articles we have shown that the electron spectral diffusion mechanism has a large influence on the electron polarizations distribution in samples presently used during DNP experiments. These distributions can be explained using a set of rate equation for the electron and nuclear polarizations, and introducing a model for taking the eSD process into account. In future studies this model will be used to explain the influence of the electron polarization distribution on the DNP enhancements, and can also be beneficial in the context of EPR spectroscopy. The resulting distribution profiles cannot be described relying on the classical TM mechanism and this should therefore not be used during the interpretation of the DNP induced nuclear enhancements observed in our samples.

Appendix A: Derivation of the electron spectral diffusion rate

In this Appendix we discuss the assumptions and some considerations leading to the form of the $\bar{w}_{j,j'}^{eSD}$ polarization exchange rates between the frequency bins given in Eq. 14. The dependence of these rates on the interaction parameters of the spin system is difficult to derive, however a dependence on the frequency differences between the electron bins, $|\omega_j - \omega_{j'}|$, the EPR line-shape, and on the bin size, $|\omega_j - \omega_{j-1}|$ can be suggested. In order to propose such a dependence we first consider the polarization exchange between two single electrons at frequencies ω'_j and $\omega'_{j'}$ in the system. This exchange process, ignoring the effect of all other interactions, depends on the magnitude of the off-diagonal dipolar flip-flop terms in the two-electron spin Hamiltonian. Electron spin flips modulating this dipolar interaction are the source of the eSD exchange process[20, 60, 62]. For a fixed electron pair the efficiency of this process is largest when the resonance frequencies of the electrons are equal and decreases for increasing frequency difference $|\omega'_j - \omega'_{j'}|$. Thus, the dependence of the exchange rate between these electrons, $w_{j,j'}^{eSD}$, on the frequency difference must have some bell shape form. Without deriving an explicit expression for the exchange rate between the electrons that can directly be transferred to the exchange rates between the bins, we assume a Lorentzian

line-shape dependence of the form

$$w^{eSD}_{j,j'} = \frac{(\Delta_{j,j'})^2}{\pi} \frac{\delta_{j,j'}}{\delta_{j,j'}^2 + (\omega'_j - \omega'_{j'})^2}, \quad (18)$$

where $2\delta_{j,j'}$ is the width of the Lorentzian and $\Delta_{j,j'}$ is a coefficient determined by the magnitude of the dipolar interaction between the electrons. Considering that the value of $\delta_{j,j'}$ is determined by the dipolar spin fluctuations, we expect that $\delta_{j,j'} < \Delta_{j,j'}$. The transformation of this expression to the polarization exchange rate between bins in real samples is not straightforward and we therefore assume that the expression for the average (macroscopic) exchange rate between the polarizations of electrons in bin j and bin j' has the same form as Eq. 18:

$$\overline{w}_{j,j'}^{eSD} = \frac{\overline{\Delta}^2}{\pi} \frac{\overline{\delta}}{\overline{\delta}^2 + (\omega_j - \omega_{j'})^2}. \quad (19)$$

Here the value of the dipolar parameter $\overline{\Delta}$ is expected to be smaller than the dipolar interaction between neighboring electrons, and the width coefficient $\overline{\delta}$ is again smaller than this value. The frequency differences become a multiple of the frequency width of the bins $|\omega_j - \omega_{j-1}|$. Eq. 19 can be simplified if $\overline{\delta} \ll |\omega_j - \omega_{j'}|$, resulting in

$$\overline{w}_{j,j'}^{eSD} = \frac{\Lambda^{eSD}}{(\omega_j - \omega_{j'})^2}, \quad (20)$$

with $\Lambda^{eSD} = \frac{\overline{\Delta}^2 \overline{\delta}}{\pi} < \overline{\Delta}^3$. This assumption is justified for the systems considered in the present study, where the value of $\overline{\Delta}$ and the bin width are both of the order of a couple of MHz.

We next consider the bin structure of our macroscopic system composed of N_e electrons, with $N_j = N_e f_j$ electrons in each of the ω_j bins. The rate of polarization exchange between the average polarizations P_j in bin j and $P_{j'}$ in bin j' depends on the number of electrons in each of these bins, N_j and $N_{j'}$, the average exchange rate between pairs of electrons, $\overline{w}_{j,j'}^{eSD}$, and the number of such electron pairs, $n_{j,j'}$. Realizing that we average over all possible polarization distributions inside each bin and that the average exchange rates inside the bins is faster than the inter-bin polarization exchange, such that at all time each bin can be described by an average P_j polarization, the macroscopic exchange rates $W_{j,j'}^{eSD}$ between the pairs of bins can be estimated to have the following dependence:

$$\begin{aligned} W_{j,j'}^{eSD} &= \overline{w}_{j,j'}^{eSD} n_{j,j'} / N_j \\ W_{j',j}^{eSD} &= \overline{w}_{j,j'}^{eSD} n_{j,j'} / N_{j'} \end{aligned} \quad (21)$$

Assuming that each electron in bin j has only a single directly exchanging electron in bin j'

, the parameter $n_{j,j'}$ can be expressed by

$$n_{j,j'} = N_e f_j f_{j'}. \quad (22)$$

and Eq. 21 can be rewritten as:

$$\begin{aligned} W_{j,j'}^{eSD} &= \overline{w}_{j,j'}^{eSD} f_{j'} \\ W_{j',j}^{eSD} &= \overline{w}_{j,j'}^{eSD} f_j \end{aligned} \quad (23)$$

Thus, without taking polarization conservation into account but leaving the Boltzmann steady state conditions, we get that the exchange dynamics between pairs of polarizations is given by

$$\frac{d}{dt} \begin{bmatrix} P_j \\ P_{j'} \end{bmatrix} = \overline{w}_{j,j'}^{eSD} \frac{1}{\epsilon_{j,j'} + 1} \begin{bmatrix} -\epsilon_{j,j'} f_{j'} & f_{j'} \\ -\epsilon_{j,j'} f_j & -f_j \end{bmatrix} \begin{bmatrix} P_j \\ P_{j'} \end{bmatrix}. \quad (24)$$

This form is identical to the form used to describe the effect of the $R_{j,j'}^{eSD}$ matrices on the polarization distribution, as given in Eq. 13, with Eq. 14 given by Eq. 20.

In future studies Eqs. 18 and 19 must be justified theoretically, and the exact dependence of the parameters in the latter (and therefore also in Eqs. 14) on the electron concentration and the bin size must be derived.

Acknowledgments

We thank Dr. Arnold Raitsimring for helpful discussions regarding the origins of electron spectral diffusion. This work was supported by the German-Israeli Project Cooperation of the DFG through a special allotment by the Ministry of Education and Research (BMBF) of the Federal republic of Germany. This research was also made possible in part by the historic generosity of the Harold Perlman Family. D.G holds the Erich Klieger Professorial Chair in Chemical Physics.

References

- [1] Overhauser, A., *Phys. Rev.*, 1953, **92**(2), 411–415.
- [2] Carver, T. R. and Slichter, C. P., *Phys. Rev.*, 1953, **92**(1), 212–213.
- [3] Jeffries, C.D., *Phys. Rev.*, 1957, **106**(1), 164–165.
- [4] Wind, R. A. and Duijvestijn, M. J. and van der Lugt, C. and Manenschijn, A. and Vriend, J., *Prog. Nuc. Mag. Res. Sp.*, 1985, **17**, 33–67.
- [5] Afeworki, M. and Vega, S. and Schaefer, J., *Macromolecules*, 1992, **25**(16), 4100–4105.
- [6] Afeworki, M. and McKay, R. A. and Schaefer, J., *Macromolecules*, 1992, **25**(16), 4084–4091.
- [7] Afeworki, M. and Schaefer, J., *Macromolecules*, 1992, **25**(16), 4092–4096.
- [8] Becerra, L. R. and Gerfen, G. J. and Temkin, R. J. and Singel, D. J. and Griffin, R. G., *Phys. Rev. Lett.*, 1993, **71**(21), 3561–3564.
- [9] Gerfen, G. J. and Becerra, L. R. and Hall, D. A. and Griffin, R. G. and Temkin, R. J. and Singel, D. J., *J. Chem. Phys.*, 1995, **102**(24), 9494.
- [10] Hall, D. A. and Maus, D.C. and Gerfen, G. J. and Inati, S. J. and Becerra, L. R. and Dahlquist, F. W. and Griffin, R. G., *Science*, 1997, **276**(5314), 930–932.
- [11] Ardenkjaer-Larsen, J. H. and Fridlund, B. and Gram, A. and Hansson, G. and Hansson, L. and Lerche, M. H. and Servin, R. and Thaning, M. and Golman, K., *Proc. Natl. Acad. Sci. U.S.A.*, 2003, **100**(18), 10158–63.
- [12] Kessenikh, A. V. and Luschikov, V. I. and Manenkov, A. A. and Taran, Y. V., *Sov. Phys. Solid State*, 1963, **5**, 321–329.
- [13] Kessenikh, A. V. and Luschikov, V. I. and Manenkov, A. A., *Sov. Phys. Solid State*, 1963, **5**, 835–837.
- [14] Kessenikh, A. V. and Manenkov, A. A. and Pyatnitskii, G. I., *Sov. Phys. Solid State*, 1964, **6**, 641–643.
- [15] Hwang, C. and Hill, D., *Phys. Rev. Lett.*, 1967, **18**(4), 110–112.
- [16] Wollan, D., *Phys. Rev. B*, 1976, **13**(9), 3671–3685.

- [17] Solomon, I., *Magnetic Resonance and Relaxation*, North-Holland, Amsterdam, 1963.
- [18] Abragam, A. and Goldman, M., *Reports Prog. Phys.*, 1978, **41**(3), 395–467.
- [19] Atsarkin, V. A. and Kessenikh, A. V., *Appl. Magn. Reson.*, 2012, **43**(1-2), 7–19.
- [20] Abragam, A., *The Principles of Nuclear Magnetism*, Oxford University Press, London, 1961.
- [21] Hovav, Y. and Feintuch, A. and Vega, S., *J. Magn. Reson.*, 2010, **207**(2), 176–189.
- [22] Hovav, Y. and Feintuch, A. and Vega, S., *J. Chem. Phys.*, 2011, **134**(7), 074509.
- [23] Karabanov, A. and van der Drift, A. and Edwards, L. J. and Kuprov, I. and Kockenberger, W., *Phys. Chem. Chem. Phys.*, 2012, **14**(8), 2658–68.
- [24] Hu, K.-N. and Debelouchina, G. T. and Smith, A. A. and Griffin, R. G., *J. Chem. Phys.*, 2011, **134**(12), 125105.
- [25] Hovav, Y. and Feintuch, A. and Vega, S., *J. Magn. Reson.*, 2012, **214**(1), 29–41.
- [26] Hovav, Y. and Levinkron, O. and Feintuch, A. and Vega, S., *Appl. Magn. Reson.*, 2012, **43**(1-2), 21–41.
- [27] Karabanov, A. and Kwiatkowski, G. and Kockenberger, W., *Appl. Magn. Reson.*, 2012, **43**(1-2), 43–58.
- [28] Thurber, K. R. and Tycko, R., *J. Chem. Phys.*, 2012, **137**(8), 084508.
- [29] Mentink-Vigier, F. and Akbey, U. and Hovav, Y. and Vega, S. and Oschkinat, H. and Feintuch, A., *J. Magn. Reson.*, 2012, **224**, 13–21.
- [30] Thurber, K. R. and Tycko, R., *Isr. J. Chem.*, 2014, **54**(1-2), 39–46.
- [31] Redfield, A. G., *Phys. Rev.*, 1955, **98**(6), 1787–1809.
- [32] Provotorov, B. N., *Sov. Phys. JETP*, 1962, **14**(5), 1126–1131.
- [33] Goldman, M., *Spin temperature and nuclear magnetic resonance in solids*, Clarendon Press, Oxford, 1970.
- [34] Abragam, A. and Borghini, M., *Prog. low temp. phys.*, 1964, **4**, 384–449.
- [35] de Boer, W., *J. Low Temp. Phys.*, 1976, **22**(1-2), 185–212.

- [36] Borghini, M. and Scheffler, K., *Phys. Rev. Lett.*, 1971, **26**(22), 1362–1365.
- [37] Cox, S. F. J. and Bouffard, V. and Goldman, M., *J. Phys. C Solid State Phys.*, 1973, **6**(5), L100–L103.
- [38] de Boer, W. and Borghini, M. and Morimoto, K. and Niinikoski, T. O. and Udo, F., *J. Low Temp. Phys.*, 1974, **15**(3-4), 249–267.
- [39] Kurdzesau, F. and van den Brandt, B. and Comment, A. and Hautle, P. and Jannin, S. and van der Klink, J. J. and Konter, J. A., *J. Phys. D-Appl. Phys.*, 2008, **41**(15), 155506.
- [40] Ardenkjaer-Larsen, J. H. and Macholl, S. and Johannesson, H., *Appl. Magn. Reson.*, 2008, **34**(3-4), 509–522.
- [41] Jannin, S. and Comment, A. and Kurdzesau, F. and Konter, J. and Hautle, P. and van den Brandt, B. and van der Klink, J. J., *J. Chem. Phys.*, 2008, **128**(24), 241102.
- [42] Lumata, L. L. and Jindal, A. K. and Merritt, M. E. and Malloy, C. R. and Sherry, A. D. and Kovacs, Z., *J. Am. Chem. Soc.*, 2011, **133**(22), 8673–80.
- [43] Lumata, L. L. and Merritt, M. E. and Malloy, C. R. and Sherry, A. D. and Kovacs, Z., *Appl. Magn. Reson.*, 2012, **43**(1-2), 69–79.
- [44] Jannin, S. and Comment, A. and Klink, J. J., *Appl. Magn. Reson.*, 2012, **43**(1-2), 59–68.
- [45] Shimon, D. and Hovav, Y. and Feintuch, A. and Goldfarb, D. and Vega, S., *Phys. Chem. Chem. Phys.*, 2012, **14**(16), 5729–43.
- [46] Banerjee, D. and Shimon, D. and Feintuch, A. and Vega, S. and Goldfarb, D., *J. Magn. Reson.*, 2013, **230**, 212–9.
- [47] Shimon, D. and Feintuch, A. and Goldfarb, D. and Vega, S., *Phys. Chem. Chem. Phys.*, 2014, **16**(14), 6687–99.
- [48] Atsarkin, V. A., *Sov. Phys. JETP*, 1970, **31**(6), 1012–1018.
- [49] Atsarkin, V. A., *Sov. Phys. JETP*, 1971, **32**(3), 421–425.
- [50] Atsarkin, V. A. and Rodak, M. I., *Sov. Phys. Usp.*, 1972, **15**(3), 251–265.
- [51] Farrar, C. T. and Hall, D. A. and Gerfen, G. J. and Inati, S. J. and Griffin, R. G., *J. Chem. Phys.*, 2001, **114**(11), 4922.
- [52] Granwehr, J. and Kockenberger, W., *Appl. Magn. Reson.*, 2008, **34**(3-4), 355–378.

- [53] Nagarajan, V. and Hovav, Y. and Feintuch, A. and Vega, S. and Goldfarb, D., *J. Chem. Phys.*, 2010, **132**(21), 214504.
- [54] Banerjee, D. and Paniagua, J. C. and Mugnaini, V. and Veciana, J. and Feintuch, A. and Pons, M. and Goldfarb, D., *Phys. Chem. Chem. Phys.*, 2011, **13**(41), 18626–37.
- [55] Siaw, T. and Fehr, M. and Lund, A. and Latimer, A. and Walker, S. A. and Edwards, D. T. and Han, S.-I., *Phys. chem. chem. phys.*, 2014, **16**(35), 18694–706.
- [56] Schosseler, P. and Wacker, Th. and Schweiger, A., *Chem. Phys. Lett.*, 1994, **224**(3-4), 319–324.
- [57] Rodak, M. I., *J. Exp. Theor. Phys.*, 1972, **34**(2), 832–42.
- [58] Klauder, J. and Anderson, P., *Phys. Rev.*, 1962, **125**(3), 912–932.
- [59] Mims, W. B., *Electron Spin Echoes*, Plenum, New York, 1972.
- [60] Raitsimring, A. M. and Salikhov, K. M. and Bychkov, S. F. and Tsvetkov, Y. D., *Sov. Phys. Solid State*, 1975, **17**(2), 303–306.
- [61] Salikhov, K. M. and Tsvetkov, Y. D., *Electron Spin-Echo Studies of Spin-Spin Interactions in Solids*, Wiley, New York, 1979.
- [62] Dzuba, S. A. and Kawamori, A., *Concepts Magn. Reson.*, 1996, **8**(1), 49–61.
- [63] Feintuch, A. and Shimon, D. and Hovav, Y. and Banerjee, D. and Kaminker, I. and Lipkin, Y. and Zibzener, K. and Epel, B. and Vega, S. and Goldfarb, D., *J. Magn. Reson.*, 2011, **209**(2), 136–41.
- [64] Borghini, M., *Phys. Rev. Lett.*, 1968, **20**(9), 419–421.
- [65] Hovav, Y. and Feintuch, A. and Vega, S. and Goldfarb, D., *J. Magn. Reson.*, 2014, **238**, 94–105.
- [66] Epel, B. and Gromov, I. and Stoll, S. and Schweiger, A. and Goldfarb, D., *Concepts Magn. Reson. Part B Magn. Reson. Eng.*, 2005, **26B**(1), 36–45.
- [67] Trukhan, S. N. and Yudanov, V. F. and Tormyshev, V. M. and Rogozhnikova, O. Y. and Trukhin, D. V. and Bowman, M. K. and Krzyaniak, M. D. and Chen, H. and Martyanov, O. N., *J. Magn. Reson.*, 2013, **233C**, 29–36.

- [68] Colombo Serra, S. and Rosso, A. and Tedoldi, F., *Phys. chem. chem. phys.*, 2012, **14**(38), 13299–308.
- [69] Colombo Serra, S. and Rosso, A. and Tedoldi, F., *Phys. chem. chem. phys.*, 2013, **15**(21), 8416–28.
- [70] Colombo Serra, S. and Filibian, M. and Carretta, P. and Rosso, A. and Tedoldi, F., *Phys. Chem. Chem. Phys.*, 2013.
- [71] Karabanov, A. and Kuprov, I. and Charnock, G. T. P. and van der Drift, A. and Edwards, L. J. and Kockenberger, W., *J. Chem. Phys.*, 2011, **135**(8), 084106.
- [72] Jeener, J., *Adv. Magn. Reson.*, 1982, **10**, 1–51.
- [73] Levitt, M. H. and Di Bari, L., *Phys. Rev. Lett.*, 1992, **69**(21), 3124–3127.
- [74] Ernst, M. and Meier, B. H., 1998, **84**, 83–121.
- [75] Abragam, A. and Goldman, M., *Nuclear Magnetism: Order and Disorder*, Clarendon Press, Oxford, 1982.
- [76] Maresch, G. G. and Weber, M. and Dubinskii, A.a. and Spiess, H.W., *Chem. Phys. Lett.*, 1992, **193**(1-3), 134–140.
- [77] Florent, M. and Kaminker, I. and Nagarajan, V.i and Goldfarb, D., *J. Magn. Reson.*, 2011, **210**(2), 192–9.
- [78] Kaminker, I. and Wilson, T. D. and Savelieff, M. G. and Hovav, Y. and Zimmermann, H. and Lu, Y. and Goldfarb, D., *J. Magn. Reson.*, 2014, **240**, 77–89.
- [79] Jeffries, C. D., *Dynamic Nuclear Orientation*, Wiley, New York, 1963.